Published in final edited form as:
J Comput Phys. 2008 November 20; 227(22): 9303–9332. doi:10.1016/j.jcp.2008.05.001.

An immersed-boundary method for flow–structure interaction in biological systems with application to phonation

Haoxiang Luo,
Department of Mechanical Engineering, Vanderbilt University, 2301 Vanderbilt Pl., Nashville, TN 37235-1592

Rajat Mittal[1],
Department of Mechanical and Aerospace Engineering, George Washington University, Washington, DC 20052

Xudong Zheng,
Department of Mechanical and Aerospace Engineering, George Washington University, Washington, DC 20052

Steven A. Bielamowicz,
Division of Otolaryngology, George Washington University, Washington, DC 20052

Raymond J. Walsh, and
Department of Anatomy and Cell Biology, George Washington University, Washington, DC 20052

James K. Hahn
Department of Computer Science, George Washington University, Washington, DC 20052

Abstract

A new numerical approach for modeling a class of flow–structure interaction problems typically encountered in biological systems is presented. In this approach, a previously developed, sharp-interface, immersed-boundary method for incompressible flows is used to model the fluid flow and a new, sharp-interface Cartesian grid, immersed boundary method is devised to solve the equations of linear viscoelasticity that governs the solid. The two solvers are coupled to model flow–structure interaction. This coupled solver has the advantage of simple grid generation and efficient computation on simple, single-block structured grids. The accuracy of the solid-mechanics solver is examined by applying it to a canonical problem. The solution methodology is then applied to the problem of laryngeal aerodynamics and vocal fold vibration during human phonation. This includes a three-dimensional eigen analysis for a multi-layered vocal fold prototype as well as two-dimensional, flow-induced vocal fold vibration in a modeled larynx. Several salient features of the aerodynamics as well as vocal-fold dynamics are presented.

Keywords

immersed-boundary method; elasticity; flow–structure interaction; bio-flow mechanics; phonation; laryngeal flow; flow-induced vibration

1Corresponding author: mittal@gwu.edu (E-mail), +1-202-994-9394 (Tel), +1-202-994-0238 (Fax).

1 Introduction

Flow–structure interaction (FSI) is a common phenomenon in biological systems. Typical examples related to biomedical engineering include the cardiovascular system (heart valves and arteries), and the larynx. The ability to computationally model the flow–structure interaction in these systems could help us understand the underlying biophysics, investigate pathologies, and potentially advance medical treatments. Structural flexibility and flow–induced deformation is also ubiquitous in nature. For instance, flow–structure interaction is a key feature in biological locomotion including fish/mammalian swimming ([1]) and insect/bird flight, and the ability to model this interaction is important in learning the underlying physics of these modes of locomotion.

One of the main challenges in developing such biophysical models is handling of the complex and moving anatomical geometries. The finite-element method (FEM) is the traditional way of dealing with complicated computational domains (e.g., [2,3]). However, grid generation and solution of the associated algebraic equations can be quite expensive. Furthermore, biological configurations present a singularly difficult proposition for such methods given the highly complex geometries, motions, deformation and material properties that are usually encountered in these configurations.

In recent years, the immersed-boundary (IB) method has gained popularity in computational fluid dynamics (CFD) for handling complex and/or moving boundaries. In the IB method, a structured, usually Cartesian, grid which does not conform to the flow boundary is used for discretizing the governing equations ([4]). Recent review on the IB method and its variants can be found in Mittal & Iaccarino [5]. Compared to the boundary-conforming structured and unstructured methods, the IB method has the advantages of simple grid generation ([4]) and ease of incorporating multigrid ([6]) and domain-decomposition based parallel algorithms [7].

The Cartesian grid based IB method has also been applied in the computation of solid mechanics. For example, Sethian & Wiegmann [8] used a type of IB method to solve linear elastostatics on arbitrary two-dimensional domains and the solution was used in an optimization procedure to iteratively improve structural design. In their approach, a level-set method was used to represent the boundaries of the solid body, and an immersed boundary method based on Li & LeVeque [9] and Li [10] was used to prescribe the discontinuities in the governing equations across the solid/void boundary. This approach allowed them to change the geometry and topology of the structure during the optimization process without modifying the underlying grid.

Udaykumar and coworkers [11,12] used an Eulerian method to simulate high-speed multimaterial impact. Their method was based on a fixed Cartesian grid and a sharp interface IB method was used to deal with large deformations of the material–material and material–void interfaces. The approach was particularly attractive in that the issues associated with severe mesh distortion and entangling, which would be faced by conventional body-conformal methods, can be circumvented.

In this paper, we present a Cartesian grid based approach for modeling a class of FSI problems typically encountered in biological applications. More specifically, we employ the previous sharp interface IB method [7,13,14] to solve the Navier–Stokes equations that govern the flow, and devise a new IB formulation that allows us to compute the linear elastodynamics of complex three-dimensional (3D) structures. FSI is accomplished by operating the two solvers in a coupled manner. Compared to the IB methods described in [8,11,12], our method can be

used for simulating dynamics of linearly elastic or viscoelastic solids as well as flow-induced deformation of such solids. The FSI solver is also designed to solve two- as well as three-dimensional problems and is therefore very well suited for high-fidelity modeling of biological configurations.

Although the IB method we present here for the 3D linear viscoelasticity is inspired from the approach developed in the context of the fluid dynamics by Mittal and coworkers [7,13,14] and therefore bears some similarity to that approach, the implementation is significantly different, especially with regard to the treatment of the traction boundary condition which is a unique feature of solid dynamics. This issue is discussed in detail in Section 2. It should also be noted that this method is different from the IB method described in Li and coworkers [9, 10] and Sethian & Wiegmann [8]. In their methods, the solution experiences discontinuities across the singular interface immersed in the domain, and the finite difference formulas involving the nodes across the interface were corrected by using Taylor's series around the interface and taking into consideration of the discontinuities. In contrast, our method is based on a ghost-cell methodology where the ghost-node value is a smooth extrapolation from the solution on the physical side of the boundary. There is no discontinuity involved at the boundary in our method. Furthermore, those methods require derivation of the correction term in the finite-difference formulas near the boundary, which in our view is inconvenient if applied to the 3D elasticity. In comparison, the finite-difference equations in our method are standard formulations and are thus much simpler.

Finally, the current method differs from the extended IB method or immersed finite element method proposed in [15,16] in that, in our formulation, (1) there is no body force imposed at the fluid/solid boundary or within the solid body, (2) only Cartesian meshes are used.

1.1 Modeling of laryngeal aerodynamics and vocal fold vibration

A particular focus of the current work is developing a computational modeling capability that can capture the physics of phonation which refers to the process of sound production in the larynx. Phonation is essentially a result of flow-induced vibration of the vocal folds (VF). Figure 1(a) shows a coronal (front-to-back) view of larynx obtained from a computed tomography (CT) scan. The image clearly shows the two vocal folds that protrude into the airway inside the larynx. During phonation, the two VFs are brought together at the midline and tightened so as to obstruct the passage of air from the lungs to the vocal tract above. Air is then forced through this laryngeal passageway (called the "glottis") due to buildup of the pressure inside the lungs, and this results in sustained flow-induced vibration of the VFs during which air is expelled into the vocal tract as an oscillatory jet called the "glottal jet". This sustained vibration and the oscillating airflow give rise to the generation and propagation of sound, and this process is called phonation. When attention is focused on the VF vibration and the jet behavior, air compressibility is often neglected and an incompressible flow can be assumed. The vocal fold itself has a complex structure as shown in Fig. 1(b), and the various constituents of the VF are known to play distinct roles in the vibratory dynamics[18].

The dynamics of the vocal folds and glottal jet are difficult to examine in experiments. Thus, despite a significant number of *in-vitro* and *in-vivo* studies [18], much remains to be understood regarding the biophysics of phonation. For example, little has been known about the unsteady vortex motions in the supraglottal region and their effect on the vocal fold vibration as well as the sound generation. A mathematical model that describes the dynamical process of phonation could complement experimental studies thereby helping us understand the physics of voice production. It may also have potential significance for examining certain voice pathologies and treating voice disorders.

In the past, a number of mathematical models of different complexity have been developed for describing the FSI process of phonation. The first study that attempted to examine the phonation physics using a fully coupled FSI approach was that of Ishizaka & Flanagan [19]. In this pioneering study, the VFs were modeled as two lumped masses and the air was treated as a one-dimensional inviscid flow. The model was extremely simple but was able to successfully demonstrate sustained flow-induced vibrations. Subsequent to this, lumped-mass models with more degrees of freedom were proposed and employed, e.g., the sixteen-mass model used by Titze [20]. Low-order models have been used with varying degrees of success to study some specific features of phonation. For example, the chaotic behavior in the VF vibration was examined by Jiang *et al.* [21] using a two-mass model.

Continuum models of the vocal folds have been employed in recent years. A two-/three-dimensional hybrid FEM model of VFs was introduced by Alipour *et al.* [22] where the VF tissues were assumed to have three layers and each layer was transversely isotropic and governed by linear viscoelasticity. Coupling this model with a two-dimensional (2D) flow solver, Alipour & Scherer [23] studied the bulging effect of the medial surface of the VFs due to glottal adduction. Rosa *et al.* [24] presented a fully 3D model in which dynamics of the three-layer and transversely isotropic VFs was coupled with an incompressible flow solver to simulate the FSI. In addition, they included the contact force during the VF closure, and the false vocal folds and laryngeal ventricles were incorporated into their simulation to better approximate the physical geometry. Both the solid dynamics and the fluid dynamics were solved using the FEM methods. Using the model, the authors examined the phase difference in the VF tissue deformation and the effect of the false VFs on the pressure distribution over the laryngeal surfaces.

Tao & Jiang [25] also recently considered a 3D VF model. Combining the model with Bernoulli's law, they investigated the anterior-posterior biphonation (simultaneous occurrence of two independent fundamental frequencies during phonation) phenomenon. Thomson *et al.* [26] used both 2D FEM simulations and experiments on a synthetic VF model to study the energy transfer from the airflow to the VF during the FSI. Hunter *et al.* [27,28] used numerical simulations to describe the dynamics of the VF abduction and adduction — the posturing movements of the VFs during phonation aside from their vibration.

All of the above models have been useful in describing the basic vibratory function of the VFs and some particular aspects of the phonation process. However, for a more detailed analysis of phonation, higher-fidelity models that can incorporate more realistic geometries and provide higher accuracy both in the fluid and solid dynamics are needed. Furthermore, in order to examine patient-specific configurations, which is key to effective treatment, an efficient method is needed for rapid modeling of a variety of configurations. In our research, we attempt to develop a continuum mechanics based methodology which can resolve a large range of temporal and spatial scales in both the VF vibration and aerodynamics. This model will be able to capture details of the vibratory characteristics as well as the flow behavior, and thus allow us to gain a deeper insight into the physics of phonation. The model is expected to eventually be used for improving the outcome of laryngeal surgeries. For example, in medialization laryngoplasty, a surgical procedure used to treat vocal fold paresis and paralysis, a uniquely configured structural implant is inserted into the diseased VF to improve its vibratory characteristics [29]. A high-fidelity computational model could potentially help surgeons predict the effect of the implant and possibly improve the success rate of this procedure [30]. This indeed is the long-term goal of the current effort.

In this paper we describe a crucial step toward that goal. We have developed a new Cartesian grid based immersed-boundary method to simulate the elastodynamics of complex elastic and viscoelastic solid structures. This solver is coupled with an existing IB method that solves the

incompressible Navier-Stokes equations. This combined method allows us to model FSI with complex geometries with relative ease. In Section 2, we describe the IB method for general viscoelastic solids subject to linear deformation. The method is validated and its accuracy is tested using a canonical problem and the grid refinement in Section 3. In Section 4.1, we apply the IB method to the problem of phonation and compute the vibration modes of a prototypical 3D VF. In Section 4.2, we couple the method with an immersed-boundary flow solver to simulate the flow-induced VF vibration in two dimensions. Summary and conclusions are given in Section 5.

2 An immersed-boundary method for linear viscoelasticity

In the following, we describe the salient features of the numerical method developed to solve the dynamical equations of a linear viscoelastic solid. We first describe the underlying methodology for solving the governing equations on a Cartesian mesh and then describe how the appropriate boundary conditions are applied over the immersed boundaries that do not conform to the Cartesian mesh.

2.1 Governing equations

Consider the unsteady Navier equation that governs the dynamics of a linear, viscoelastic solid

$$\rho_s \frac{\partial^2 u_i}{\partial t^2} = \frac{\partial \sigma_{ij}}{\partial x_j}, \tag{1}$$

where ρ_s is the density of the solid, u_i is the displacement, and σ_{ij} is the stress tensor. The body force is ignored in the equation. In general, if the Kelvin–Voigt model [31] is assumed for the viscous effect, the constitutive law between the stress and the strain can be written as

$$\sigma_{ij} = C_{ijmn}\varepsilon_{mn} + \eta_{ijmn}\dot{\varepsilon}_{mn}, \tag{2}$$

where C_{ijmn} is the elasticity tensor, η_{ijmn} is the damping coefficient, $\varepsilon_{mn} = (\partial u_m/\partial x_n + \partial u_n/\partial x_m)/2$ is the strain tensor, and the dot represents the time derivative. Note that in this paper, we use x, y, z as well as the indicial values 1, 2, 3 interchangeably for ease of discussion.

If the material of the solid is transversely isotropic and elastic, then the constitutive relationship is reduced to

$$\begin{bmatrix} \varepsilon_{xx} \\ \varepsilon_{yy} \\ \varepsilon_{zz} \\ \varepsilon_{yz} \\ \varepsilon_{zx} \\ \varepsilon_{xy} \end{bmatrix} = \begin{bmatrix} \frac{1}{E_p} & -\frac{\nu_p}{E_p} & -\frac{\nu_{zp}}{E_z} & 0 & 0 & 0 \\ -\frac{\nu_p}{E_p} & \frac{1}{E_p} & -\frac{\nu_{zp}}{E_z} & 0 & 0 & 0 \\ -\frac{\nu_{pz}}{E_p} & -\frac{\nu_{pz}}{E_p} & \frac{1}{E_z} & 0 & 0 & 0 \\ 0 & 0 & 0 & \frac{1}{2G_{zp}} & 0 & 0 \\ 0 & 0 & 0 & 0 & \frac{1}{2G_{zp}} & 0 \\ 0 & 0 & 0 & 0 & 0 & \frac{1}{2G_{xy}} \end{bmatrix} \cdot \begin{bmatrix} \sigma_{xx} \\ \sigma_{yy} \\ \sigma_{zz} \\ \sigma_{yz} \\ \sigma_{zx} \\ \sigma_{xy} \end{bmatrix}, \tag{3}$$

where the xy plane is the isotropic plane, E_p, G_{xy}, and ν_p are the Young's modulus, shear modulus, and Poisson ratio in the xy plane, respectively, E_z, G_{zp}, and ν_{pz} are the Young's modulus, shear modulus, and Poisson ratio in the z direction, respectively, and these are related as follows:

$$G_{xy} = \frac{E_p}{2(1+\nu_p)}, \quad \frac{\nu_{pz}}{E_p} = \frac{\nu_{zp}}{E_z}.$$

The 6×6 matrix in (3) is the compliance matrix. The principal stresses are related to the strain by

$$\begin{bmatrix} \sigma_{xx} \\ \sigma_{yy} \\ \sigma_{zz} \end{bmatrix} = \begin{bmatrix} k_{xx} & k_{xy} & k_{xz} \\ k_{yx} & k_{yy} & k_{yz} \\ k_{zx} & k_{zy} & k_{zz} \end{bmatrix} \begin{bmatrix} \varepsilon_{xx} \\ \varepsilon_{yy} \\ \varepsilon_{zz} \end{bmatrix}, \tag{4}$$

where k_{ij} are the elements of the inverse of the 3×3 partition at the upper left corner of the compliance matrix.

A second-order, implicit Crank–Nicolson scheme is employed for temporal discretization of (1) which leads to the following semi-discrete equation:

$$\rho_s \left(\frac{u_i^{n+1} - 2u_i^n + u_i^{n-1}}{\Delta t^2} \right) = \frac{\partial}{\partial x_j} \left[\frac{C_{ijmn}}{2} (\varepsilon_{mn}^{n+1} + \varepsilon_{mn}^{n-1}) \right] + \frac{\partial}{\partial x_j} \left[\eta_{ijmn} \left(\frac{\varepsilon_{mn}^{n+1} - \varepsilon_{mn}^{n-1}}{2\Delta t} \right) \right], \tag{5}$$

where the superscripts represent the time levels. The above equation can be rewritten as

$$u_i^{n+1} - \frac{\Delta t^2}{2\rho_s} \frac{\partial}{\partial x_j} \left[(C_{ijmn} + \frac{\eta_{ijmn}}{\Delta t}) \varepsilon_{mn}^{n+1} \right] = 2u_i^n - u_i^{n-1} + \frac{\Delta t^2}{2\rho_s} \frac{\partial}{\partial x_j} \left[(C_{ijmn} - \frac{\eta_{ijmn}}{\Delta t}) \varepsilon_{mn}^{n-1} \right], \tag{6}$$

which shows that the discrete equation has to to be inverted at each time step. Note that for static problems, we simply solve the equilibrium equation

$$\frac{\partial}{\partial x_j} [C_{ijmn} \varepsilon_{mn}] = 0. \tag{7}$$

All the spatial derivatives in the governing equations are approximated using a second-order, centered finite-difference scheme. For example, the $\partial \sigma_{xx}/\partial x$ term in Eq. (1) for a transversely isotropic and elastic material, on a uniform Cartesian grid would be discretized as follows:

$$\begin{aligned} \frac{\partial \sigma_{xx}}{\partial_x} &= \frac{\partial (k_{xx}\varepsilon_{xx} + k_{xy}\varepsilon_{yy} + k_{xz}\varepsilon_{zz})}{\partial x} \\ &= \frac{1}{\Delta x} \left[k_{xx_{i+\frac{1}{2},j,k}} \frac{u_{x_{i+1,j,k}} - u_{x_{i,j,k}}}{\Delta x} - k_{xx_{i-\frac{1}{2},j,k}} \frac{u_{x_{i,j,k}} - u_{x_{i-1,j,k}}}{\Delta x} \right] \\ &+ \frac{1}{2\Delta x} \left[k_{xy_{i+1,j,k}} \frac{u_{y_{i+1,j+1,k}} - u_{y_{i+1,j-1,k}}}{2\Delta y} - k_{xy_{i-1,j,k}} \frac{u_{y_{i-1,j+1,k}} - u_{y_{i-1,j-1,k}}}{2\Delta y} \right] \\ &+ \frac{1}{2\Delta x} \left[k_{xz_{i+1,j,k}} \frac{u_{z_{i+1,j,k+1}} - u_{z_{i+1,j,k-1}}}{2\Delta z} - k_{xz_{i-1,j,k}} \frac{u_{z_{i-1,j,k+1}} - u_{z_{i-1,j,k-1}}}{2\Delta z} \right], \end{aligned} \tag{8}$$

where Δ_x, Δ_y, and Δ_z are the grid sizes in the x, y, and z directions, respectively, $k_{xx_{i+\frac{1}{2},j,k}}$ is the average of $k_{xx_{i,j,k}}$ and $k_{xx_{i+,j,k}}$, and so on. Similar expressions can be obtained for the other derivative terms. A key point to note is that the discretized equation has a 9-point point stencil as shown in Fig. 2 for 2D problems and a 19-point stencil for 3D problems.

2.2 Boundary conditions

The viscoelastic solids under consideration are subject to two types of boundary conditions: a displacement boundary condition

$$u_i = U_i, \tag{9}$$

where U_i is the specified boundary displacement, and a traction boundary condition

$$\sigma_{ij} n_j = f_i, \tag{10}$$

where n_j is the surface normal pointing out of the solid, and f_i is the surface traction as shown in Fig. 3. In the body-conformal grid methods, the boundary conditions are usually easy to apply and do not introduce any significant complexity into the numerical methodology. With a non-body-conformal Cartesian grid such as the current one, the imposition of these boundary conditions is not trivial and the methodology adopted to implement these boundary conditions is the crux of the current immersed-boundary method.

2.3 Immersed-boundary formulation

Inspired by the sharp-interface IB method for CFD described in [7,13,14], we devise a method to solve the equations (1)–(10) with complex geometries on Cartesian grids. The method is described here mostly within the context of a 2D problem, but as will be demonstrated later in the paper, the method is generally applicable to 3D problems. As shown in Fig. 3, the solid body is immersed in a Cartesian grid. For cells inside the solid which are away from the boundary, the governing equations are discretized as shown in Fig. 2 where the displacement vector u_i is defined at the cell centers. Near the immersed boundary, the governing equations need the boundary conditions, and since the immersed boundary does not conform with the grid, a methodology is needed to incorporate the influence of the boundary conditions on the governing equations. Following [7,13,14], we employ a ghost-cell methodology for imposing the boundary conditions. The basic idea behind this method is as follows

1. We first identify so called “ghost-cells” which are the cells outside the solid that lie within the computational stencil of the cells inside the solid. In Fig. 4 the ghost-cells are indicated with square symbols.
2. We then devise a numerical prescription for the ghost-cell nodal values to incorporate the boundary condition in the vicinity of the ghost-cell.
3. Once this is accomplished, the governing equations for the cells inside the solid can be solved in a coupled manner with the numerical prescription for the ghost-cell values which leads to imposition of the boundary conditions on the immersed boundary.

In the current solver, the surface of the immersed body is represented by a grid made up of triangular elements. The use of the triangular mesh gives us a flexible and robust way of representing highly complex geometries and also facilitates computation of the surface quantities such as the local normals. The methodology used to identify the ghost-cells (denoted as ‘GC’ in Fig. 4) on a Cartesian grid for such immersed bodies is described in previous publications [7,13] and will not be discussed here. The focus of the current discussion will be the technique used to incorporate the effect of the displacement and traction boundary conditions within the context of the current immersed-boundary methodology.

Regardless of the type of boundary condition to be applied, we first identify a location on the immersed boundary, unique to each ghost-cell, where the boundary condition will be satisfied. A natural choice for this location is the point on the immersed boundary which is closest to the

given ghost-cell, and this is determined by computing the normal body-intercept (denoted by 'BI') for the ghost-cell. With the point determined uniquely, we now turn to describing the methodology for imposing the different boundary conditions at this location using the ghost-cell methodology.

The displacement boundary condition is the more straightforward of the two, and for this we employ a method that is similar to what has been done in the context of fluid dynamics [7, 13,14]. The normal segment from the ghost-cell to the body-intercept point is extended into the solid to a point called the image-point (denoted by 'IP') such that distance between GC and BI is the same as the distance between IP and BI. Thus, the BI point lies at the center of the segment between GC and IP (Fig. 4).

Next, we identify the four (eight in 3D) nodes that surround the image-point (the shaded square region shown in Fig. 4(*a*)) and express the variable under consideration (for discussion sake, we consider a generic variable, ϕ) in terms of a bilinear (trilinear in 3D) interpolant of the form

$$\phi(x,y)=\alpha_1 xy+\alpha_2 x+\alpha_3 y+\alpha_4, \tag{11}$$

where α's are the weights that can be expressed in terms of the values at the surrounding nodes. The final expression for the value of the variable at the image-point can be written as

$$\phi_{IP}=\sum_{i=1}^{M}\beta_i\phi_i, \tag{12}$$

where ϕ_i is the value of ϕ at the ith vertex and β_i is the interpolation weight. The integer M is equal to 4 for 2D simulations and 8 for 3D simulations. Note that the interpolation may involve the ghost-node of interest or other nearby ghost-nodes, but as pointed out in [7], this does not cause any particular problem for the methodology. The Dirichlet-type boundary condition is then enforced at the body-intercept point using a second-order approximation along the surface normal,

$$\phi_{GC}+\phi_{IP}=2\phi_{BI}, \tag{13}$$

where ϕ_{GC} denotes the variable value at the ghost-node and ϕ_{BI} denotes the boundary condition at the boundary interception. The final equation that governs the value at the ghost-node can be written as

$$\phi_{GC}+\sum_{i=1}^{M}\beta_i\phi_i=2\phi_{BI}. \tag{14}$$

Thus, the value at the ghost-node is coupled with the adjoining solid and in some cases other ghost-nodes, and is also directly connected with the boundary condition at the body-intercept point. These equations for the ghost-nodes can then be solved in a fully coupled or loosely coupled manner with the governing equations for the solid on the interior nodes.

The traction boundary condition for solids, Eq. (10), is more complicated since it involves both the normal and tangential gradients of the displacement vector, and as will be shown below, its application on the solid is a unique feature that has to be developed for the current immersed-boundary method. The problem within the current context comes down to impose $\sigma_{ij}n_j = f_i$ at

the body-intercept point with adequate accuracy. The methodology adopted should also be robust and amenable to a fast solution procedure. To illustrate the complexity of this problem, we assume that the solid is isotropic, linearly elastic and has deformation only in the *xy* plane (i.e. a plane-strain condition). Transforming the coordinate system into the local orthogonal coordinates involving the surface normal and tangential vectors as shown in Fig. 4 (*b*), the traction condition becomes

$$\sigma_{nn}=k_{xx}\frac{\partial u_n}{\partial \mathbf{n}}+k_{xy}\frac{\partial u_\xi}{\partial \xi}=f_n,\ \ \sigma_{\xi n}=G_{xy}\left(\frac{\partial u_n}{\partial \xi}+\frac{\partial u_\xi}{\partial \mathbf{n}}\right)=f_\xi. \tag{15}$$

where the subscripts, *n* and ξ, represent the normal and tangential components of a vector.

It can be noted now that the traction boundary condition not only involves partial derivatives in the normal and tangential directions, it also couples the various components of the displacement vector. One possible approach to imposing (15) is to draw analogy from the Neumann boundary condition treatment developed for the pressure Poisson equation in CFD [7,13]. In this method, we start with a bi- or tri-linear (in 3D) approximation for the variable at the image-point and then approximate the normal derivative of a generic variable, ϕ, using the following second-order accurate, central-difference formula

$$\frac{\partial \phi}{\partial \mathbf{n}}\Big|_{BI}=\frac{\phi GC-\phi IP}{\Delta l_p}, \tag{16}$$

where Δl_p is the distance between GC and IP.

For the tangential derivative, $\partial\phi/\partial\xi$, at the BI, we may again use a bilinear (as in Eq. (11)) or trilinear interpolant for the variable in a region around the body-intercept point. However, this approach leads to a number of problems. First, the body-intercept might not lie inside the square or rectangle formed by the four nodes that surround the image-point. For such cases, the four nodes surrounding the body-intercept point may involve a number of ghost-nodes. This situation is illustrated schematically in Fig. 4(*b*) where three of the four nodes surrounding the BI point are ghost-nodes. This has two deleterious effects: it strengthens the coupling between the ghost-cell under consideration and neighboring ghost-cells, and diminishes the coupling between this ghost-cell and the interior of the solid. This in turn has a negative impact on the convergence properties of the successive over-relaxation (SOR) iterative solver used for obtaining the solution of the governing equations. The bilinear interpolation can also lead to estimates of the tangential derivative that are of reduced accuracy. Accurate estimation of the tangential derivative requires an interpolation scheme that incorporates substantial information from regions that are located tangentially on either sides of the body-intercept point. However, in the current bilinear interpolation, most of the points involved in the interpolation are located in a region that is nominally normal to the BI. Thus, approximations to the tangential derivative obtained from the bilinear interpolation scheme described above can be inaccurate. Thus, a method is needed for the traction boundary condition which is accurate, robust, and does not negatively impact the convergence properties of the iterative solution procedure. Here we describe a methodology which has been developed to handle this boundary condition. Motivated by the explicit jump immersed-boundary method described in [8,10], we introduce a two- (or three-dimensional), third-order polynomial, Φ, to approximate the generic function ϕ in the neighborhood of the BI point, (x_0, y_0, z_0),

$$\phi(\hat{x},\hat{y},\hat{z}) \approx \Phi(\hat{x},\hat{y},\hat{z}) = \sum_{l=0}^{3}\sum_{j=0}^{3}\sum_{i=0}^{3} c_{ijl}\,\hat{x}^i\hat{y}^j\hat{z}^l,\ i+j+l \le 3, \tag{17}$$

where $\hat{x} = x - x_0$, $\hat{y} = y - y_0$, $\hat{z} = z - z_0$, and c_{ijl} are unknown coefficients. For 2D problems, there are 10 coefficients, and for 3D problems, the number of these coefficients is 20. To determine c_{ijl}, we first draw a circle (or a sphere in 3D) of radius R centered at the point (x_0, y_0, z_0) as shown in Fig. 5, and select N nodes enclosed by the circle/sphere. The polynomial Φ is then required to satisfy a weighted least-squares error criterion. That is, c_{ijl} are chosen to minimize the error ϵ given by

$$\epsilon = \sum_{n=1}^{N} w_n^2 [\Phi(\hat{x}_n,\hat{y}_n,\hat{z}_n) - \phi(\hat{x}_n,\hat{y}_n,\hat{z}_n)]^2, \tag{18}$$

where ($\hat{x}_n$, $\hat{y}_n$, $\hat{z}_n$) is the nth data point, and w_n is the weight function. For the least-squares problem to be well posed, we require $N \ge 10$ for 2D cases and $N \ge 20$ for 3D cases. For each BI point, we adaptively adjust R so that the required number of data points are included. Typically, the circle/sphere will contain solid nodes and ghost-nodes as shown in Fig. 5. Except for the ghost-node associated with the BI point under consideration, we choose not to include any of the other ghost-nodes into the data fitting scheme. This removes any direct coupling between the ghost-nodes and is essential to ensure robust convergence in the iterative solution process. Thus, the final set of nodes included in the function approximation scheme are the ghost-node under consideration and the N-1 solid nodes. For the particular case shown in Fig. 5, the nodes included in the approximation are shown with crosses in for a 2D case.

A weight function needs to be chosen to complete the prescription, and here we follow the work of Li[10] and use the following cosine weight function,

$$w_n = \frac{1}{2}\left[1+\cos\left(\frac{\pi d_n}{R}\right)\right], \tag{19}$$

where $d_n = \sqrt{\hat{x}^2+\hat{y}^2+\hat{z}^2} \le R$ is the distance between the nth data point and the body-intercept. The exact solution to (18) is then given in a compact form,

$$\mathbf{c} = (\mathbf{WV})^{\perp}\mathbf{W}\phi = \left(\mathbf{V^T W^2 V}\right)^{-1}\mathbf{V^T W^2}\phi, \tag{20}$$

where $\perp$ represents the pseudoinverse of a matrix, the vector $\mathbf{c}$ contains the coefficients c_{ijl}, the vector $\boldsymbol{\phi}$ contains the data $\boldsymbol{\phi}(\hat{x}_n, \hat{y}_n, \hat{z}_n)$, $\mathbf{W}$ and $\mathbf{V}$ are the weight and Vandermonde matrices given by

$$\mathbf{W} = \begin{bmatrix} w_1 & & & \\ & w_2 & & \\ & & \ddots & \\ & & & w_N \end{bmatrix},\ \mathbf{V} = \begin{bmatrix} 1 & x_1 & y_1 & z_1 & x_1^2 & y_1^2 & z_1^2 & \cdots \\ & & & \cdots & & & & \\ 1 & x_n & y_n & z_n & x_n^2 & y_n^2 & z_n^2 & \cdots \\ & & & \cdots & & & & \\ 1 & x_N & y_N & z_N & x_N^2 & y_N^2 & z_N^2 & \cdots \end{bmatrix}. \tag{21}$$

Note that **V** has the dimension of $N \times 20$ in 3D and $N \times 10$ in 2D. Given the geometry of the body and the grid, c_{ijl} can be written as a linear combination of $\phi(\hat{x}_n, \hat{y}_n, \hat{z}_n)$ based on Eq. (20).

For every ghost-node associated with the traction boundary, three polynomials are obtained by solving the data fitting problems to approximate the three components of the displacement u_i, and thus the displacement gradient tensor $\partial u_i/\partial x_j$ at the BI point is obtained in terms of c_{ijl} by differentiating the approximating polynomials at $(\hat{x}, \hat{y}, \hat{z}) = (0, 0, 0)$ analytically,

$$\frac{\partial \mathbf{\Phi}}{\partial x}\Big|_{(0,0,0)} = c_{100},\ \frac{\partial \mathbf{\Phi}}{\partial y}\Big|_{(0,0,0)} = c_{010},\ \frac{\partial \mathbf{\Phi}}{\partial z}\Big|_{(0,0,0)} = c_{001}. \tag{22}$$

Substituting the expressions and Eq. (20) into the traction condition $\sigma_{ij}n_j = f_i$, we obtain a linear equation expressing the boundary condition at (x_0, y_0, z_0), and the equation involves the displacements u_i at the data points including the associated ghost-node.

Discretizing Eq. (6) at N_I interior nodes in the solid body using the finite-difference scheme, we obtain (for 3D) $3N_I$ linear equations for the displacement u_i. If there are totally N_G ghost-nodes, then $3N_G$ complementary equations are obtained by imposing either displacement or traction boundary condition at the BI points corresponding to the ghost-nodes using the aforementioned methodology. The assembled linear system can be written in a compact form

$$\begin{bmatrix} \mathbf{A}_{11} & \mathbf{A}_{12} \\ \mathbf{A}_{21} & \mathbf{A}_{22} \end{bmatrix} \cdot \begin{bmatrix} \mathbf{u}_I \\ \mathbf{u}_G \end{bmatrix} = \begin{bmatrix} \mathbf{r} \\ \mathbf{s} \end{bmatrix}, \tag{23}$$

where $\mathbf{u}_I$ and $\mathbf{u}_G$ are vectors encapsulating the displacements at interior nodes and ghost-nodes, A_{ij} are matrix partitions arising from discretization, **r** is the right-hand side of (6), and **s** is the vector encapsulating the prescribed boundary displacement U_i and the external force f_i at the BI points. Note that for static problems, a system similar to (23) is obtained except that $\mathbf{r} = \mathbf{0}$ for these problems.

Equation (23) is solved in an iterative manner wherein the interior and ghost-node values are updated in a sequential manner until convergence. This method is notionally described as follows:

$$\mathbf{A}_{11} \cdot \mathbf{u}_I^{(k)} = \mathbf{r} - \mathbf{A}_{12} \cdot \mathbf{u}_G^{(k-1)},\ \mathbf{A}_{22} \cdot \mathbf{u}_G^{(k)} = \mathbf{s} - \mathbf{A}_{21} \cdot \mathbf{u}_I^{(k)}, \tag{24}$$

where the first equation is the update of the interior (solid) nodes and the second is the update of the ghost-nodes. In the above equations, the superscript *k* represents the iteration level. In present paper, we use the point-SOR method to solve the first sub-equation. Other iteration methods, such as line-SOR, BiCGSTAB and GMRES (e.g., [32]), could also be implemented in a straightforward manner if needed. The second sub-equation is also solved by updating each ghost-node using the Gauss–Seidel method and typically requires only a few iterations.

In summary, the current method does not compute any explicit jump-conditions as in [8] since it does not treat the body surface as a discontinuity in an otherwise continuous field. Rather, ghost-nodes are employed to impose the boundary conditions precisely at the exact location of the boundary. Thus the current method can be considered a “sharp-interface” method within the lexicon of the immersed-boundary methods [5,33,34].

2.4 Formulation of eigenvalue problems

The present immersed-boundary method may be also be used to formulate an eigenvalue problem for an elastic solid which is an extremely useful feature for analysis of solid dynamics. For this analysis we assume that Eq. (1) is subject to homogeneous boundary conditions and zero damping, and its solution has the form $\mathbf{u}(\mathbf{x}, t) = \hat{\mathbf{u}}(\mathbf{x})e^{i\omega t}$ where $\hat{\mathbf{u}}$ is the eigenfunction encapsulating the three components of the displacement vector at all the interior nodes and ghost-nodes, i is the imaginary unit, and ω is the eigenfrequency. Substituting this solution into (1), we may then write the discrete version of this equation in a matrix form as

$$\begin{bmatrix} \mathbf{A}_1 & \mathbf{A}_2 \\ \mathbf{A}_3 & \mathbf{A}_4 \end{bmatrix} \cdot \begin{bmatrix} \hat{\mathbf{u}}_I \\ \hat{\mathbf{u}}_G \end{bmatrix} = -\rho_s w^2 \begin{bmatrix} \mathbf{I} & 0 \\ 0 & 0 \end{bmatrix} \cdot \begin{bmatrix} \hat{\mathbf{u}}_I \\ \hat{\mathbf{u}}_G \end{bmatrix}, \tag{25}$$

where $\hat{\mathbf{u}}_I$, $\hat{\mathbf{u}}_G$ are the displacement eigenmodes at the interior nodes and ghost-nodes, respectively, and $\mathbf{A}_i$ are matrices arising from the discretization. It should be noted that the second line of the equation, which encapsulates $3N_G$ sub-equations, corresponds to the displacement or traction boundary condition associated with each ghost-node. Equation (25) poses a generalized algebraic eigenvalue problem which can be solved using standard algorithms such as the Implicitly Restarted Arnoldi Method (IRAM) adopted by the software ARPACK [35]. Note that for this software package, there is no need to store or process the large matrices in (25) during the eigensolution process. Rather, only the matrix–vector product is needed, and this can be efficiently calculated on the Cartesian grid.

With the description of the method complete, we now present results of simulations conducted using the immersed-boundary, solid-dynamics solver. The solver is designed to solve the equations for small deformations of linear viscoelastic solids. The solver can be used for solid-dynamics, eigenanalysis, as well as flow-induced deformation of such solids, and example of each of these is provided in order to demonstrate the capabilities of the solver.

3 Grid refinement study

The spatial accuracy of the linear-elastic solver as well as its fidelity is examined by computing the numerical solution for a non-trivial geometry on different grids and comparing with a known exact solution. Here we consider an infinitely long annulus with inner radius R_1 and outer radius R_2 as shown in Fig. 6 (*a*). The outer surface of the annulus is displaced in the radial direction by distance *s*, and the inner surface is either fixed (i.e., zero displacement) or free (i.e., zero traction). For both these conditions, an exact solution can be obtained if we limit ourselves to a static, linearly elastic problem (e.g., [36]). In this case, the elastostatics is reduced to the axisymmetric plane-strain Lamé equation whose exact solution for the radial displacement *d* at radius *r* is given by

$$d(r) = -\frac{A}{2G}\frac{1}{r} + \frac{2\nu C}{\lambda} r, \tag{26}$$

where $\lambda = \nu E/(1 - \nu - 2\nu^2)$, and $G = E/(2 + 2\nu)$ are the two Lamé constants, *E* and ν are the Young's modulus and Poisson ratio, respectively, *A* and *C* are two constants given by

$$A = \frac{2GR_1^2R_2}{R_2^2 - R_1^2}s, \quad C = \frac{A}{2R_1^2(1 - 2\nu)} \tag{27}$$

if the inner surface is fixed (zero displacement), or

$$A = -\frac{2GR_1^2R_2}{R_1^2+(1-2\nu)R_2^2}s,\ C = -\frac{A}{2R_1^2} \tag{28}$$

if the inner surface is traction-free.

Figure 6(*a*) shows the 2D Cartesian grid used for solving the elastostatics of the annulus, and Fig. 6(*b*) shows the contours of the radial displacement in the *xy* coordinates obtained on a 96 × 96 uniform grid for the free inner surface and $E = 1$, $\nu = 0.35$, $R_2 = 1$, $R_1 = 0.5$, $s = 0.05$. The radial displacement function is shown in Fig. 6 (*c*) where it is found that the numerical solution has excellent agreement with the exact solution.

Figure 7 shows the L_2 and infinity norms of the relative error of the solutions for both cases. The numerical method clearly shows a second-order convergence rate as the number of grids is increased for both types of boundary conditions, thereby confirming the formal accuracy of the solver.

4 Application to Phonation

Histologically, the vocal fold consists of the vocalis muscles and mucosa, and the mucosa is comprised of the epithelium at the surface and the lamina propria below, as shown in Fig. 1 (*b*). At the VF edge, the lamina propria can be further divided into three layers: the superficial, intermediate, and deep layers. From a mechanical point of view, these layers may be regrouped into three layers: the cover (the epithelium and superficial layer of the lamina propria); the ligament (the intermediate and deep layers of lamina propria); and the body (vocalis muscles) [17].

The geometrical model of the VF in the present study is shown in Fig. 8 where the undeformed VF prototype is uniform in the longitudinal direction (*z* direction) in which the muscle fibers are aligned. The *x*, *y*, and *z* coordinates represent the vertical, lateral, and anterior-posterior directions, respectively, in terms of human anatomy. The three layers in the cross section are illustrated in Fig. 8 (*b*) and their geometries are roughly based on the anatomical data shown in Fig. 1. The details of the VF geometry are given in the appendix. The VF chosen for analysis is 1 cm in height, 0.99 cm in width, and 1.4 cm in length, which are nominal values for adult humans [22,37]. We assume that the VF undergoes small deformations so that linear theory may apply. This assumption is considered appropriate for phonation and has been employed in past studies (e.g., [22,24]). Each of the three layers is assumed to be isotropic in the cross section transverse to the direction of the VF muscle fibers.

4.1 Eigenmode analysis of vocal folds

We choose the material properties of each layer based on the values from Alipour *et al.* [22], and they are listed in Table 1. Note that Alipour *et al.* [22] did not specify the longitudinal Young's moduli, E_z and, since the longitudinal Poisson ratios were assumed to be zero in their FEM model, the effect of the VF stretching on the deformation is ignored in their analysis.

Using the immersed-boundary method, we solve the eigenvalue problem in (25) for the VF prototype to obtain four lowest eigenfrequencies. The anterior, posterior, and lateral surfaces of the VF shown in Fig. 8(*a*) are attached to the cartilage and have zero displacement. The remaining surface of the VF is assumed to be traction-free. Since the eigenmode analysis does not involve any interaction between the two VFs, we only conduct the eigenmode analysis for one VF and present the results for both by reflecting the results about the central line of symmetry. The grid size of 20 × 20 × 12 is employed in the *x*, *y* and *z* directions, and grid

sensitivity studies indicate that this relatively coarse grid is adequate for the current eigenmode analysis. The present number of grid is significantly higher than that of Alipour *et al.* [22] where about 150 mesh points were used. Fig. 9 shows the lowest two eigenmodes, mode-1 and 2, and their corresponding shape in the mid coronal plane. The associated eigenfrequencies are 114 Hz and 125 Hz. As shown in the midplane, mode-1 primarily entails an oscillation of the VF in the vertical direction, whereas mode-2 represents an oscillation in the lateral direction. It should be noted that both modes produce significant opening and closing of glottis which is the airway between the two VFs.

The next two modes, mode-3 and 4, are shown in Fig. 10. The eigenfrequencies associated with these modes are 133 Hz and 144 Hz. The two modes represent more complex deformations in the vertical and lateral direction. In both modes, the oscillations involve the alternate widening/narrowing of the supraglottal gap and the subglottal gap. This wave-like modes are similar to those observed *in-vivo* by means of high-speed cinematography [38]. It should be noted that the fundamental frequency of vocal vibration for adult males can vary from 65 Hz to 260 Hz and has a typical value of 130 Hz [38]. Thus the present results are in a realistic range, which provides some level of validation for the current modeling procedure. Furthermore, given that the first four modes are all within the acceptable range of frequencies, the eigenmode analysis cannot definitively be used to predict which mode or modes will occur during phonation. In fact, more than one mode may be present during phonation, but this can only be examined by conducting a FSI study.

It is worthwhile to compare the results from the current eigenmode analysis with that of Alipour *et al.* [22]. We note that the first three eigenfrequencies obtained in their study were 137, 165, and 195 Hz, which are more widely separated on the spectrum compared to our results. However, their mode shapes agree qualitatively with those presented by us. The differences in the eigenfrequencies are acceptable considering the significant difference in the VF geometry. The VF prototype they used was thinner (x direction) and tapered in width (y direction) from the posterior end to the anterior end, and their profile of each tissue layer is also different than ours. In addition, they assumed that the Poisson ratio v_{pz} was zero so that the longitudinal stretching of the VF does not cause any deformation in the coronal plane. This assumption, which is somewhat *ad-hoc*, is not employed in the current study.

4.2 Flow-induced vocal fold vibration

While the eigenmode analysis described above is useful in that it provides insight into the natural modes of the VF vibration that can be expected during phonation, it cannot predict the actual vibratory characteristics during phonation. This can only be obtained from a coupled FSI study. Here we have carried out a simulation of FSI of the vocal folds that attempts to model both the VF dynamics and the fluid dynamics with high fidelity. The FSI modeling is accomplished by coupling the current solid-dynamics IB method with an existing IB flow solver. In this Section, we describe the salient features of this coupled solution process and present results from the FSI study. The current FSI study is limited to a 2D configuration.

4.2.1 Immersed-boundary flow solver—Here we provide a very brief overview of the incompressible IB solver used in the current simulations. Further details regarding the solver are available in [13,14]. A straightforward dimensional analysis based on the transglottal pressure and air density given in Section 4.2.3 shows that the laryngeal flow velocity is on order of 30 m/s and the Mach number is thus about 0.1. Therefore, the flow is essentially incompressible. The governing equations for the flow solver are the incompressible Navier–Stokes equation and the continuity equation,

$$\begin{aligned} \frac{\partial v_i}{\partial t}+\frac{\partial v_j v_i}{\partial x_j} &= -\frac{1}{\rho_a}\frac{\partial p}{\partial x_i}+\nu_a\frac{\partial^2 v_i}{\partial x_j^2}, \\ \frac{\partial v_i}{\partial x_i} &= 0, \end{aligned} \tag{29}$$

where v_i is the velocity, ρ_a and v_a are the air density and viscosity, and p is the aerodynamic pressure. No-slip and no-penetration conditions are specified at the flow/solid boundary. Equation (29) is solved on a non-uniform Cartesian grid.

The flow/solid boundary is represented by an unstructured surface mesh with triangular elements. All spatial derivatives are approximated with a second-order central difference scheme on the grid. The discretized field equations are evaluated at the collocation points inside the flow domain. Near the immersed boundary, ghost-nodes are identified and a second-order interpolation scheme is used to satisfy the boundary conditions on the body. The boundary conditions are imposed at the exact location of the physical flow/solid interface, more specifically, at the body-intercept points obtained by projecting the ghost-nodes onto the flow/solid boundary.

The unsteady Navier–Stokes equation is marched in time using a fractional-step scheme which involves two steps: an advection-diffusion equation followed by a pressure Poisson equation. During the first step, both the viscous terms and convective terms are treated implicitly using the Crank– Nicolson scheme to improve the stability. In the cases of moving boundaries, the surface marker points and ghost-nodes are updated at the beginning of each time step.

4.2.2 Coupling of the flow and solid-dynamics solvers—In simulating the flow–structure interaction, we couple the Navier–Stokes equation, (29), together with the governing equation for viscoelasticity of solid bodies, (1). Both equations are discretized on their own Cartesian grids using the finite-difference method, but they share the unstructured surface mesh that represents the interface between the flow and the solids. Both grids immerse this surface, and on each grid, a set of ghost-cells are defined and projected onto the interface to facilitate the implementation of the boundary condition for each solver using the immersed-boundary method. The two governing equations are coupled such that

$$\begin{aligned} v_i^{\text{fluid}}\big|_{\Gamma'} &= v_i^{\text{solid}}\big|_{\Gamma}, \\ \sigma_{ij}^{\text{solid}}\, n_j\big|_{\Gamma'} &= \sigma_{ij}^{\text{fluid}}\, n_j\big|_{\Gamma'} = f_i^{\text{fluid}}\big|_{\Gamma'}, \end{aligned} \tag{30}$$

where Γ represents the undeformed fluid/solid interface, and Γ' represents the deformed interface. The use of this mixed formulation (undeformed for solid and deformed for fluid) needs some explanation. The underlying assumption in solid-dynamics solver is that the deformations are are small and in the linear range. Within this context, although the solid exhibits displacement and deformation, the change in shape of the solid due to this displacement and deformation is not accounted for in the computation of the solid-dynamics. This approach is standard and consistent with the underlying linear, small deformation assumption [36] for the solid and has also been used in the past for VF modeling [22,24,37]. Thus, the solid-dynamics solver does not have to contend with a moving boundary. On the other hand, the displacement of the VF surface is explicitly accounted for in the fluid-flow simulation. The motion of the VF, although small, is the crucial element in its interaction with the fluid and in the generation of a complex, pulsatile glottal jet. Thus, for the fluid-flow simulations, we track the motion of the surface elements as the VF deforms and impose the no-slip, no-penetration boundary conditions on the deformed surface of the boundary at each time step.

In the flow solver, as the boundary moves, the nodal points on the fixed Cartesian grid may emerge into the fluid or disappear from the fluid. The method of dealing this issue is given by Mittal *et al.* [14] and is not discussed here. On the other hand, such an issue does not exist in the present solid-dynamics solver since the linear elasticity is assumed and the physical boundary of the elastic body remains stationary during the simulation.

The coupling between the fluid and solid solvers is explicit. That is, at each time step, the flow is marched by one step with current deformed shape and velocities of fluid/solid interface as the boundary conditions. The aerodynamic forces imparted on the VF are then calculated at current location of the marker points via an interpolation scheme on the flow grid. Finally, the solid is marched by one step with the updated forces, and the deformation and velocities on the solid grid are interpolated onto the marker points, so that the fluid/solid interface is updated. This explicit coupling is quite simple, robust and efficient, and is found to work well for the VF vibration problem. As will be shown later, the explicit coupling does not in anyway impact the stability or the time-step requirements of the solver. Implicit coupling, if needed, can be easily incorporated by iterating between the fluid and solid solvers at each time step.

4.2.3 Simulation setup—We apply the numerical approach to the flow–structure interaction problem of phonation where both the flow and VFs are assumed to be two-dimensional, and we furthermore assume a plane- strain deformation (i.e., deformation restricted in the coronal plane). The computational domain is shown in Fig. 11. A pair of VFs are placed symmetrically in a straight channel, and their geometry, including the inner layer profiles, is the same as the cross section of the 3D prototype shown in Fig. 8.

All dimensions are chosen based nominally on anatomical data [17]. The channel length and width are $L = 12$ cm and $H = 2$ cm, respectively. The initial gap between the VFs is 0.02 cm. The flow goes from left to right and is driven by a constant pressure drop $\Delta P = P_{\text{in}} - P_{\text{out}}$, where P_{in} and P_{out} are the gage pressure at the inlet and the exit of the channel, respectively.

No-slip and no-penetration boundary conditions for the flow are imposed both on the VF/flow interface and on the channel walls. At the inlet and exit, pressure is held constant, and a zero streamwise gradient boundary condition, $\partial v_i/\partial_x = 0$, is specified for the velocity. In all simulations, we assume that $P_{\text{in}} = 1$ kPa, $P_{\text{out}} = 0$, and the air density is $\rho_a = 0.001$ g/cm^3. Note that in reality, subglottal pressure is 0.2 to 0.3 kPa to sustain phonation for low vocal intensities, and may go as high as 1.5 to 2 kPa for loud speech [38]. Thus the current value may be considered intermediate between the two extremes. The exit pressure is set at the atmospheric level to approximate the flow condition at the end of the vocal tract. The channel is chosen to be long enough so that such an approximation is expected to have a minimal effect on the flow/VFs interaction.

The longitudinal stretching and 3D shear in the VFs during deformation due to anterior/posterior attachment to the cartilage can not be directly incorporated into the current 2D model. We therefore choose to strengthen the VFs by changing the modulus of elasticity of the material such that the lowest eigenfrequency produced by the 2D model is close to that of the 3D model in Section 4.1. The 2D VFs are also assumed to be isotropic, and their material properties are listed in Table 2.

In order to confirm that this stiffening procedure does not introduce any spurious effects, we have conducted an eigenmode analysis of the stiffened 2D VFs. The lowest four eigenmodes of the 2D vocal fold have frequencies of 94 Hz, 215 Hz, 247 Hz, and 424 Hz, and they are shown in Fig. 12. Compared to the mid-plane deformation of the modes shown in Fig. 9 and Fig. 10, it can be seen that the shapes of first three 2D modes are very close to their 3D counterparts, even though the eigenfrequencies are quite different except for the first mode.

As will be shown in next Section, such a 2D model still produces many realistic features of phonation.

We introduce a simple, linear viscoelastic model by reducing the constitutive law in (3) to

$$\begin{aligned} \sigma_{xx} &= k_{xx}\varepsilon_{xx}+k_{xy}\varepsilon_{yy}+\eta\dot{\varepsilon}_{xx},\ \sigma_{yy}=k_{yx}\varepsilon_{xx}+k_{yy}\varepsilon_{yy}+\eta\dot{\varepsilon}_{yy}, \\ \sigma_{xy} &= 2G_{xy}\varepsilon_{xy}+\eta\dot{\varepsilon}_{xy}, \end{aligned} \tag{31}$$

where η is the tissue viscosity. There is some level of uncertainty about the typical value of tissue viscosity. For instance, Alipour *et al.* [22] used values ranging from 3 to 5 poise (p) whereas Rosa *et al.* [24] used values ranging from 10 to 150 p. In the current study we have chosen two different values of the tissue viscosity, η = 6 and 10 p which allow us to clearly delineate the effect of this important parameter.

The Cartesian grid for the flow solver covers the entire computational domain, and the VFs are immersed in the grid, as shown in Fig. 13. In the *x* direction, the grid is divided into three regions, as shown in Table 3. In Region II, the grid is uniform, while Regions I and III, the grid is gradually coarsened toward to the end of the domain. A total number of 288 grid points is used in this direction whereas 256 uniformly distributed grid points are used in the *y* direction. We define the Reynolds number based on the flow rate $Re_Q = (3/2)Q/\nu_a$, where $Q = \int v_1\, dy$ is the volume flux per unit span. Alternatively, we may define the Reynolds number based on the centerline velocity and the channel width, $Re_c = (1/2)U_cH/\nu_a$, where U_c is the peak centerline velocity at the glottal exit. As will be discussed in next Section, these values for the current simulation are $Re_Q \sim 300$ and $Re_c \sim 2000$.

The Cartesian grid for the solid solver that immerses both vocal folds has a resolution of 50 in *x* and 100 in *y*, and is uniform in both directions. The non-homogeneous material properties are inserted onto the Cartesian grid nodes, and no additional effort is made to more precisely delineate the interior boundaries of the multi-layered vocal fold. This approximation is reasonable considering the inherent uncertainty in the exact geometry of each layer in the VF tissues. To deal with contact between the two VFs during glottal closure, we apply a simple kinematic constraint on the VFs that enforces a minimum glottal gap of 0.02 cm which is a small fraction of the maximum glottal gap. A higher-fidelity contact model is currently being developed and will be used for future simulations.

The size of the time step is restricted by the numerical stability of the flow solver which dictates a maximum Courant-Friedrichs-Lewy (CFL) number of about 3.0. In present simulations, we choose $\Delta t = 5\times10^{-4}$ centi-second (cs) and this leads to about 1000 to 2000 time steps in every vibration cycle. It should be noted that the explicit coupling between the fluid and solid solvers does not limit the time-step size for stable computation. It is also worthwhile to note that the computation of the solid dynamics in the present simulations represents only a small fraction of the total CPU time which is dominated by the solution of the fluid dynamics. Overall, one cycle of the VF vibration takes about 15 CPU hours on one processor of a 1.8 MHz AMD Opteron™ workstation.

To examine the sensitivity of our simulation results to the grid resolution and time-step size, we have doubled the number of grids in the region near the VFs for the flow solver and also doubled the grids of the solid-dynamics solver. The time step is also reduced by about half to maintain the same maximum CFL number. As will be presented in the next Section, the finer mesh simulation shows no significant difference in the vibration modes and frequencies, and also exhibits post-glottal fluid dynamics similar to the nominal grid case. We thus conclude that the current grid as well as the chosen time-step size are sufficient to accurately resolve the fluid/solid dynamics of the problem.

4.2.4 Simulation results—Figure 14 shows the history of the glottal gap width for the two cases which clearly indicates a transient state that eventually develops into a stationary state representing sustained vibrations. The vibration amplitude grows slowly to 0.11 cm for the η = 10 p case and 0.2 cm for the η = 6 p case. In the first few cycles, the vibration frequency is approximately 100 Hz. However this is found to change gradually to about 210 Hz as the vibrations reach a stationary state. This behavior is found to occur for both cases. It is noted that these two frequencies are very close to the first and second eigenfrequencies of the 2D solid body. Further inspection of the vibration shows that at the onset of the vibration, the VFs are displaced in the *x* direction due to the mean pressure force in the streamwise direction. Subsequently, the VFs oscillate back and forth in a manner similar to the first eigenmode shown in Fig. 12(*a*). Gradually, the *x*-direction vibration is reduced, and the VFs then start to displace more in the *y* direction, thereby opening and closing in a way found to be qualitatively similar to the second eigenmode shown in Fig. 12(*b*). This mode continues to grow until a steady state is reached. Therefore, both the frequency and the vibration mode imply that, during the flow–structure interaction, the first eigenmode of the VFs is the one that is excited initially, but then the second eigenmode is triggered and dominates the stationary state of the vibration.

Some laryngoscopic studies[38] suggest that the glottis may change from a converging shape during the opening phase to a diverging shape during the closing phase. However, our current FSI model does not indicate the presence of this mode of vibration (which, based on our eigenmode analysis, is mode-3 shown in Fig. 12(*c*)). It is useful to discuss this in detail since it points to some open questions in the computational modeling of the VF vibrations.

It should be pointed out that our FSI results are consistent with our eigenmode analysis of the VF model which shows that mode-2 (see Fig. 12(*b*)) is a lateral mode where all lateral displacement are in phase with each other and mode-3 (see Fig. 12(*c*)) is the converging-diverging mode. Thus, it is expected that mode-2 would likely dominate over mode-3 in the FSI modeling. So the questions now are: why does the in-phase mode (mode-2) occur before the converging-diverging mode (mode-3) in our model, and what does that imply about the modeling procedure? As a detailed examination of literature shows, the answers to these questions are not straightforward.

First and foremost, the relative order of these two modes depends on the shape and material properties assumed for the vocal folds. For instance, Berry & Titze [39] showed an eigenmode spectrum for their continuum VF model which has precisely the same ordering as ours when they assumed the tissue to be compressible. However, they found that mode-2 and mode-3 switch order when the tissue is made nearly incompressible. Similarly, Cook & Mongeau [40] have shown that the modes switch order as the aspect-ratio (length over width) of the vocal folds is varied. Finally, both Ishizaka [41] and Zhang *et al.* [42] showed that mode-2 and mode-3 “entrain” (converge to the same frequency) as the jet flow velocity is increased. Thus, the implication from this is that our eigenmodes merely reflect the particular VF model that we have chosen, and our FSI model is consistent with the eigenmodes and therefore with the model that we have assumed for the current study.

Second, many past studies, especially those employing two-mass models, have been contrived in a way as to produce the converging-diverging mode. For instance, Tao *et al.* [43] and LaMar *et al.* [44] used two-mass models where only the lower mass is exposed to the aerodynamic force. Thus, the upper mass is driven only indirectly by the lower mass, and this necessarily generates a phase difference between the oscillations of the two masses and thereby produces the converging-diverging mode.

It should be pointed out that the sustained frequency of 210 Hz found in our simulations is relatively high, but is still within the range of the fundamental human phonation frequency

which varies from 65 Hz to 260 Hz [38]. Therefore, the flow can be considered a reasonable approximation of phonatory flow. We have found that the eigenfrequencies for the 3D vocal fold model are distributed over a narrower band than the the 2D modes. Therefore, in full 3D simulations which will be pursued in our future work, a similar mode transition behavior, if it occurs, would be less drastic than that in present simulations.

A typical waveform of the glottal volume flow is adapted from [18] and is shown in the schematic in Fig. 15. The waveform indicates a slow rise in the volume flux followed by a rapid fall. The shape of the waveform is important since it helps determine not only the acoustic power in the sound generation but also the quality of the sound [18]. Following [18], we define T as the period of a vibration cycle, T_0 as the duration of flow, T_p and T_n as the rising and dropping phases of Q, Q_{max} and Q_{mean} as the maximum and mean of the volume flow. These quantities are shown in Fig. 15. We also define the shape-dependent parameters, $\tau_0 = T_0/T$ as the open quotient, $\tau_s = T_p/T_n$ as the skewing quotient, and $q_r = Q_{mean}/Q_{max}$.

Figure 16 shows the volume flux of the airflow, Q, for η = 6 and 10 p, together with the phase of the glottal gap represented by the dotted line. The characteristic quantities of the waveform for the two cases are listed in Table 4. For comparison, the simulation results on the refined grids are also tabulated, which confirm the sufficiency of the present grid resolution. For η = 10 p, τ_0 is 0.61 and τ_s is 1.33, whereas for the η = 6 p, τ_0 is 0.55 and τ_s is 1.60. The typical established values of τ_0 range from about 0.4 to 0.7 [18], and therefore the present results are quite reasonable.

The skewness of the waveform of the volume flux as parameterized in terms of τ_s, is also consistent with previous studies especially given that waveforms presented in literature seems to show a wide variation. For instance, LaMar *et al.* [44] who employed a two-mass model found τ_s values ranging from about 1.1 to 1.3. The seminal work of Ishizaka & Flanagan [19] on the other hand (which also employed a two-mass model) predicted a large value of τ_s of 3.4. Value of τ_s from the simulations of Duncan *et al.* [45] which employed a multi-mass model are estimated (from plots in the paper) to vary from about 1.3 to about 1.9. Our computed values of τ_s, which vary from 1.33 to 1.6, are therefore in the range observed in past studies.

The mean flow rate during normal phonation measured in experiments is typically between 110 to 220 cm^3/s [38]. In present 2D simulations, the mean flow rate is estimated to be $157 cm^2/s$ for the first case and 268 cm^2/s for the second case. Considering that the longitudinal glottal opening has an oval shape and is order of 1 cm in length, the current calculations are in the correct range. In the current simulations, the leakage flow rate during the VF closure is about 12 cm^2/s which is less than 3% of the peak flow rate for both cases. Thus, the narrow opening that remains due to our kinematic contact model produces a virtually negligible magnitude of leakage flow. It is interesting to note that even healthy larynges can have incomplete closure during phonation leading to flow leakage [18].

The peak Reynolds numbers based on the flow rate are Re_Q = 300 and Re_Q = 570 for η = 10 and 6 p, respectively. The corresponding peak Reynolds numbers based on the centerline velocity and channel width are Re_c = 2550 and 3120, respectively. In adult humans, effective Reynolds number of the glottal flow can attain peak values of about Re_Q = 3000 [18] and are expected to be lower in children. Past studies have employed Reynolds number (based on our current definition) ranging from about $Re_Q \approx 1000$ in [46] to $Re_Q \approx 3000$ in [47]. However, the detailed flow motions were not presented in those work. The vibratory characteristics of the VFs are expected to be relatively insensitive to the Reynolds number and the lower Reynolds number in the current study alleviates the grid requirements while still producing relevant results.

Figure 17 and Figure 18 show a sequence of instantaneous spanwise vorticity contours for η = 10 p which reveal details of the flow dynamics during the sustained vibration. It can be seen that when the VFs are open, the fluid is pushed out by the subglottal pressure into the supraglottal region leading to the formation of the so-called “glottal jet”. It is interesting that the jet shows significant asymmetry and may be deflected to either one side of the channel. This is because there are strong flow recirculations in the downstream channel created in previous cycles which tend to turn the glottal jet one way or the other. The sequence of plots also show that the direction of the jet deflection may change from one cycle to another depending on the particular condition of the downstream circulation as shown in Fig. 17 and Fig. 18. In our simulations, we did not observe a periodic pattern in the cycle-to-cycle jet deflection, which indicates a stochastic nature to this phenomenon.

Steady channel flow with a sudden expansion is known to have a bifurcation in its solution at a critical Reynolds number which depends on the expansion ratio [48]. Beyond the bifurcation point, the symmetric solution becomes unstable and the steady flow may become asymmetric even though the geometry is symmetric, similar to the flow patterns shown in Fig. 17 and Fig. 18. According to [48], the symmetry-breaking takes place at the critical Reynolds number based on the flow rate $Re = (3/2)Q/\nu = 26$ when the expansion ratio is 10. In addition, the critical Reynolds number is reduced when the expansion ratio increases. In present paper, the expansion ratio varies between 10 and 100 during a vibration cycle and the jet Reynolds number is much higher than the critical Reynolds number. Therefore, the flow is operating under the conditions that would produce an asymmetric solution. Furthermore, the Reynolds number is high enough for the present flow to be unsteady even if the geometry were stationary. Interestingly, jet asymmetry in the form of a Coanda effect has also been observed in experiments and simulations that attempt to model the glottal flow ([49–51]). Thus it seems that jet asymmetry is a general feature of these flows. However, the experiments [51] also show clearly the transition to turbulence of the glottal jet and that phenomenon is not captured in the current 2D laminar simulations.

To date, little is known about the distribution of pressure across the glottis during phonation since this information is very difficult to obtain *in-vivo*. Knowledge of the pressure distribution however is crucial not only for developing better insight into the glottal flow dynamics, it is also key in the development of low-order models for VF dynamics (e.g., [52,53]). Figure 19 shows the gage pressure distribution along the channel centerline for the η = 10 p case. When the glottis is closed (Fig. 19a), the pressure is nearly constant in the subglottal region, and rapidly approaches the zero supraglottal value across the glottis. Therefore, though the flow passage during the glottis is never completely closed in our simulations, the VFs still function well in providing effective blockage between the supraglottal and subglottal regions. During the stage when the VFs are open (Fig. 19b), pressure exhibits a somewhat gradual drop before again dropping sharply, and then reaches a minimum in the glottis. This result qualitatively agrees with the measurement on a static VF model in Scherer *et al.* [52] and with the FSI simulation of Tao *et al.* [43]. The instantaneous pressure immediately downstream the vocal folds shows significant variations due to the unsteady flow motion, which is not discussed in [43,52].

Typical velocity field around the glottis during the open phase is shown in Fig. 20. The medial surfaces of the two VFs form a divergent channel when the glottis is fully open. The included angle is about 10° for η = 10 p, and 20° for η = 6 p. For the former case, the flow is nearly symmetric in the glottis and separates at the glottal exit. Note that the flow becomes asymmetric as it enters the supraglottal expansion. For the latter case, separation occurs within the glottis, and the flow detaches from the VF surface. The location of the separation point changes during the VF vibration. It may move to the glottal exit as the VFs close up, re-appear or switch to

the other side of the glottis in the next cycle. Similar phenomena have been reported in the experimental observation in [51], where a flow at higher Reynolds number was studied.

The vorticity plots in Fig. 17 and Fig. 18 show that the flow is not periodic, even though the global mass flux shown in Fig. 14(*b*) is nearly periodic. To further investigate the temporal features of the flow, we plot in Fig. 21, the time-traces of the flow velocity components, v_1 and v_2, at the point $x = 4.5$ cm on the centerline for the $\eta = 10$ p case. Both components exhibit highly irregular oscillations during the VF vibration, indicating a chaotic behavior of the flow. Multiple time scales in the flow are also evident. The dominant scale is the period of the VF vibration, $T \approx 0.5$ cs. In addition, time-scales associated with the Kelvin–Helmholtz instability of the shear layers that comprise the glottal jet are also found in the flow. However, the large excursions in the jet direction make it difficult to identify this frequency.

Figure 22(*a*) shows the time-averaged streamline pattern of the flow for the $\eta = 10$ p case, and Fig. 22(*b*) shows the averaged v_1 velocity profiles at different locations along the *x*-axis. A pair of large recirculation zones reside on the two sides of the jet, and a smaller secondary pair of vortices are located at the corners of the VFs. It should be noted that even though the average is take over about 15 cycles, the mean flow is still asymmetric about the channel centerline. This is due to the stochastic nature and large time-scales that are present in the supraglottal region. The averaged streamlines indicate a rapid expansion in the jet as it enters the supraglottal region. However this is actually a result of the stochastic cycle-to-cycle deflection that is seen in the glottal jet.

The mechanical stress in the VFs is important since the VF tissues may experience fatigue and damage due to the excessive stress. In extreme cases, excessive and prolonged stress can cause laryngeal pathologies such as VF nodules [54]. Figure 23 shows the three stress components, σ_{xx}, σ_{yy}, and σ_{xy} for $\eta = 10$ p when the VFs are fully open. In the *x* direction, the VFs are compressed since σ_{xx} is negative. The maximal compression is about 1 kPa and takes place at the vocal fold base. The sign of σ_{yy} indicates that the VFs are compressed on the supraglottal side, and are slightly stretched on the subglottal side. The maximal compression reaches 5 kPa. The shear stress, σ_{xy}, is concentrated at the VF base and the subglottal portion of the cover layer, where σ_{xy} is about 0.8 kPa.

5 Conclusions

We have developed a numerical approach to simulate a class of flow–structure interaction typically encountered in biological systems. A new sharp-interface IB methodology has been developed to solve the elastodynamics of a linear viscoelastic solid. The key feature in the development of the IB methodology for elastodynamics is a robust and efficient formulation for imposing the traction boundary condition on the solid surface. This newly developed elastodynamic solver is coupled to an existing sharp-interface IB flow solver in order to simulate flow–structure interaction.

The elastodynamic solver is validated and its accuracy is examined by solving a canonical problem for which the exact solution exists. Based on this test, it is confirmed that the elastodynamic solver is locally and globally second-order accurate in space. We have applied the IB method to simulate laryngeal aerodynamics and vocal fold vibration during phonation. In this paper, air-flow is modeled as an incompressible flow driven by a constant subglottal pressure, and vocal fold tissues are represented by a transversely isotropic and multi-layer structure governed by linear viscoelasticity.

The eigenmodes of a simplified three-dimensional vocal fold prototype are computed using the new immersed-boundary method. The eigenfrequencies obtained are found to be in a range

typical for normal human phonation. The corresponding eigenfunctions provide good insights into the type of modes expected in even simple VF models.

A two-dimensional model is used for the flow-induced vocal fold vibration study. These simulations capture several important features of phonation. First, self-sustained vocal fold vibrations whose frequency lies in the range of normal human phonation are obtained. Second, the temporal patterns of the glottal opening and volume flux measures are reasonably realistic. Third, the simulations suggest that the VF vibration undergoes a distinct transition at the start of phonation. The transient stage is dominated by the mode that closely resembles the first mode identified in the eigenmode analysis, whereas the stationary stage is identified more closely with the second eigenmode.

The flow structures reveal that in the simplified geometry, the glottal jet is skewed due to the downstream flow recirculation. The range of time-scales present in the supraglottal flow results in a highly non-periodic variation in the flow, and this is manifested most dramatically in stochastic cycle-to-cycle deflection of the glottal jet.

Although there are a number of assumptions inherent in our model, the current simulations represent a step forward towards the development of higher-fidelity biomechanical models of the human larynx. Work is currently ongoing to introduce ever more realism in the model including three-dimensional CT based laryngeal geometries, higher Reynolds numbers, and a more accurate model of the VF collision. Results from these new models will be presented in the future.

A Description of the VF model used in current study

Here we provide details regarding the geometry of the vocal folds employed in the current simulations. It is expected that description of these details will facilitate comparison with future studies by other researchers. The profile of each layer is described by two polynomials in the coordinate system as shown in Fig. 8 (*b*)

$$\begin{aligned} y(x) &= 2.304x^3+0.552x^2, \quad \text{when } x \le 0, \\ y(x) &= -34.2x^2, \quad \text{when } x>0, \end{aligned} \tag{32}$$

for the cover;

$$\begin{aligned} y(x) &= 3.047x^3+0.883x^2+0.085x - 0.097, \quad \text{when } x \le -0.1, \\ y(x) &= -183.489x^3 - 46.698x^2 - 3.835x - 0.2, \quad \text{when } x> - 0.1, \end{aligned} \tag{33}$$

for the ligament; and

$$\begin{aligned} y(x) &= 4.388x^3+1.509x^2+0.170x - 0.194, \quad \text{when } x \le -0.1, \\ y(x) &= 29.351x^3 - 6.845x^2 - 2.250x - 0.327, \quad \text{when } x> - 0.1, \end{aligned} \tag{34}$$

for the body. The lateral side is located at $y = -0.99$ cm.

Acknowledgments

We want to acknowledge Dr. Haibo Dong for his help in understanding the flow solver. This research is supported by NIDCD grant R01 DC007125-01A1. Support from the GW Institute of Biomedical Engineering is also gratefully acknowledged.

References

1. Mittal R. Computational modeling in biohydrodynamics: Trends, challenges, and recent advances. IEEE J. of Oceanic Eng 2004;29(3):595–604.
2. Tezduyar TE, Aliabadi SK, Behr M, Mittal S. Massively parallel finite element simulation of compressible and incompressible flows. Comput. Methods Appl. Mech. Engrg 1994;119:157–177.
3. Bathe M, Kamm RD. A fluid-structure interaction finite element analysis of pulsatile blood flow through a compliant stenotic artery. J. Biomech. Eng 1999;121(4):361–369. [PubMed: 10464689]
4. Peskin CS. Flow patterns around heart valves: a numerical method. J. Comput. Phys 1972;10:252–271.
5. Mittal R, Iaccarino G. Immersed boundary methods. Annu. Rev. Fluid Mech 2005;37:239–261.
6. Udaykumar HS, Mittal R, Rampunggoon P, Khanna A. A sharp interface cartesian grid method for simulating flows with complex moving boundaries. J. Comput. Physics 2001;174:345–380.
7. Ghias R, Mittal R, Dong H. A sharp interface immersed boundary method for com-pressible viscous flows. J. Comput. Phy. Accepted.
8. Sethian JA, Wiegmann A. Structual boundary design via level set and immersed boundary methods. J. Comput. Phy 2000;163:489–528.
9. LeVeque RJ, Li Z. The immersed interface method for elliptic equations with discontinuous coefficients and singular sources. SIAM J. Numer. Anal 1994;31(4):1019–1044.
10. Li Z. A fast interative algorithm for elliptic interface problems. SIAM J. Numer. Anal 1998;35(1): 230–254.
11. Udaykumar HS, Tran L, Belk DM, Vanden KJ. An eulerian method for computation of multimaterial impact with eno shock-capturing and sharp interfaces. J. Comput. Phy 2003;186:136–177.
12. Tran LB, Udaykumar HS. A particle-level set-based sharp interface cartesian grid method for impact, penetration, and void collapse. J. Comput. Phy 2004;193:469–510.
13. Dong H, Mittal R, Najjar FM. Wake topology and hydrodynamic performance of low-aspect-ratio flapping foils. J. Fluid Mech 2006;566:309–343.
14. Mittal R, Dong H, Bozkurttas M, Najjar FM, Vargas A, vonLoebbeck A. A versatile sharp interface immersed boundary method for incompressible flows with complex boundaries. J. Comput. Phy. 2007Accepted.
15. Wang X, Liu WK. Extended immersed boundary method using fem and rkpm. Comput. Methods Appl. Mech Engrg 2004;193:1305–1321.
16. Zhang L, Gerstenberger A, Wang X, Liu WK. Immersed finite element method. Comput. Methods Appl. Mech Engrg 2004;193:2051–2067.
17. Hirano, M.; Sato, K. Histological Color Atlas of the Human larynx. San Diego: Singular Publishing Group; 1993.
18. Titze, IR. Principles of voice production. Englewood Cliffs, NJ: Prentice-Hall; 1994.
19. Ishizaka K, Flanagan JL. Synthesis of voiced sounds from a two-mass model of the vocal cords. Bell System Tech. J 1972;51:1233–1268.
20. Titze IR. The human vocal cords: a mathematical model, part i. Phonetica 1973;28:129–170. [PubMed: 4788091]
21. Jiang JJ, Zhang Y, Stern J. Modeling of chaotic vibrations in symmetric vocal folds. J. Acoust. Soc. Am 2001;110(4):2120–2128. [PubMed: 11681389]
22. Alipour F, Berry DA, Titze IR. A finite-element model of vocal-fold vibration. J. Acoust. Soc. Am 2000;14:442–454.
23. Alipour F, Scherer RC. Vocal fold bulging effects on phonation using a biophysical computer model. J. Voice 2000;14(4):470–483. [PubMed: 11130105]
24. Rosa MO, Pereira JC, Grellet M, Alwan A. A contribution to simulating a three-dimensional larynx model using the fine element method. J. Acoust. Soc. Am 2003;114(5):2893–2905. [PubMed: 14650023]
25. Tao C, Jiang JJ. Anterior-posterior biphonation in a finite element model of vocal fold vibration. J. Acoust. Soc. Am 2006;120(3):1570–1577. [PubMed: 17004479]

26. Thomson SL, Mongeau L, Frankel SH. Aerodynamic transfer of energy to the vocal folds. J. Acoust. Soc. Am 2005;118(3):1689–1700. [PubMed: 16240827]
27. Hunter EJ, Titze IR, Alipour F. A three-dimensional model of vocal fold abduction/adduction. J. Acoust. Soc. Am 2004;115(4):1747–1759. [PubMed: 15101653]
28. Titze IR, Hunter EJ. A two-dimensional biomechanical model of vocal fold posturing. J. Acoust. Soc. Am 2007;121(4):2254–2260. [PubMed: 17471739]
29. Koufman JA. Laryngoplasty for vocal cord medialization: an alternative to teflon. Laryngo-scope 1986;96:726–731.
30. Anderson TD, Spiegel JR, Sataloff RT. Thyroplasty revisions: frequency and predictive factors. J. Voice 2003;17:442–448. [PubMed: 14513967]
31. Fung, YC. Biomechanics. Vol. 2nd edition. New York: Springer–Verlag; 1993.
32. Press, WH.; Teukolsky, SA.; Vetterling, WT.; Flannery, BP. Numerical Recipes 3rd Edition: The Art of Scientific Computing. Cambridge University Press; 2007.
33. Ye T, Mittal R, Udaykumar HS, Shyy W. An accurate cartesian grid method for simulation of viscous incompressible flows with complex immersed boundaries. J. Comput. Phys 1999;156:209–240.
34. Marella S, Krishnan S, Liu H, Udaykumar HS. Sharp interface cartesian grid method i: an easily implemented technique for 3d moving boundary computations. J. Comput. Phy 2005;210:1–31.
35. Lehoucq, RB.; Sorensen, DC.; Yang, C. ARPACK users' guide: solution of large-Scale eigenvalue problems with implicitly restarted Arnoldi methods. Philadephia: SIAM; 1997. (Also available online)
36. Fung, YC. Foundations of solid mechanics. Englewood Cliffs, NJ: Prentice-Hall; 1965.
37. Gunter H. A mechanical model of vocal-fold collision with high spatial and temporal resolution. J. Acoust. Soc. Am 2003;113:994–1000. [PubMed: 12597193]
38. Zemlin, WR. Prentice Hall. Vol. 3rd edition. Englewood Cliffs, NJ: Prentice Hall; 1988. Speech and hearing science: anatomy & physiology.
39. Berry DA, Titze IR. Normal modes in a continuum model of vocal fold tissues. J. Acoust. Soc. Am 1996;100(5):3345–3354. [PubMed: 8914316]
40. Cook DD, Mongeau L. Sensitivity of a continuum vocal fold model to geometric parameters, constraints, and boundary conditions. J. Acoust. Soc. Am 2007;121(4):2247–2253. [PubMed: 17471738]
41. Ishizaka, K. Equivalent lumped-mass models of vocal folds vibration. In: Stevens, KN.; Hirano, M., editors. Vocal Fold Physiology. Tokyo: University of Tokyo; 1981. p. 231-244.
42. Zhang Z, Neubauer J, Berry DA. Physical mechanisms of phonation onset: A linear stability analysis of an aeroelastic continuum model of phonation. J. Acoust. Soc. Am 2007;122(4):2279–2295. [PubMed: 17902864]
43. Tao C, Zhang Y, Hottinger DG, Jiang JJ. Asymmetric airflow and vibration induced by the Coanda effect in a symmetric model of the vocal folds. J. Acoust. Soc. Am 2007;122(4):2270–2278. [PubMed: 17902863]
44. LaMar MD, Qi Y, Xina J. Modeling vocal fold motion with a hydrodynamic semicontinuum model. J. Acoust. Soc. Am 2003;114(1):455–464. [PubMed: 12880056]
45. Duncan C, Zhai G, Scherer R. Modeling coupled aerodynamics and vocal fold dynamics using immersed boundary methods. J. Acoust. Soc. Am 2006;120(5):2859–2871. [PubMed: 17139744]
46. Alipour F, Scherer RC. Flow separation in a computational oscillating vocal fold model. J. Acoust. Soc. Am 2004;116(3):1710–1719. [PubMed: 15478438]
47. Alipour F, Fan C, Scherer RC. Numerical simulation of laryngeal flow in a forced-oscillation glottal model. Computer Speech and Language 1996;10:75–93.
48. Drikakis D. Bifurcation phenomena in incompressible sudden expansion flows. Phys. Fluids 1997;9 (1):76–87.
49. Erath BD, Plesniak MW. An investigation of bimodal jet trajectory in flow through scaled models of the human vocal tract. Experiments in Fluids 2006;40:683–696.
50. Suh J, Frankel SH, Mongeau L, Plesniak MW. Computational aeroacoustics of flow through static model of human vocal tract. J. Acoust. Soc. Am 2006;119(5):3303.

51. Neubauer J, Zhang Z, Miraghaie R, Berry DA. Coherent structures of the near field flow in a self-oscillating physical model of the vocal folds. J. Acoust. Soc. Am 2007;121(2):1102–1118. [PubMed: 17348532]

52. Scherer RC, Shinwari D, De Witt KJ, Zhang C, Kucinschi BR, Afjeh AA. Intraglottal pressure profiles for a symmetric and oblique glottis with a divergence angle of 10 degrees. J. Acoust. Soc. Am 2001;109(4):1616–1630. [PubMed: 11325132]

53. Alipour F, Scherer RC. Dynamic glottal pressures in an excised hemilarynx model. J. Voice 2000;14 (4):443–454. [PubMed: 11130103]

54. Titze IR. Mechanical stress in phonation. J. Voice 1994;8(2):99–105. [PubMed: 8061776]

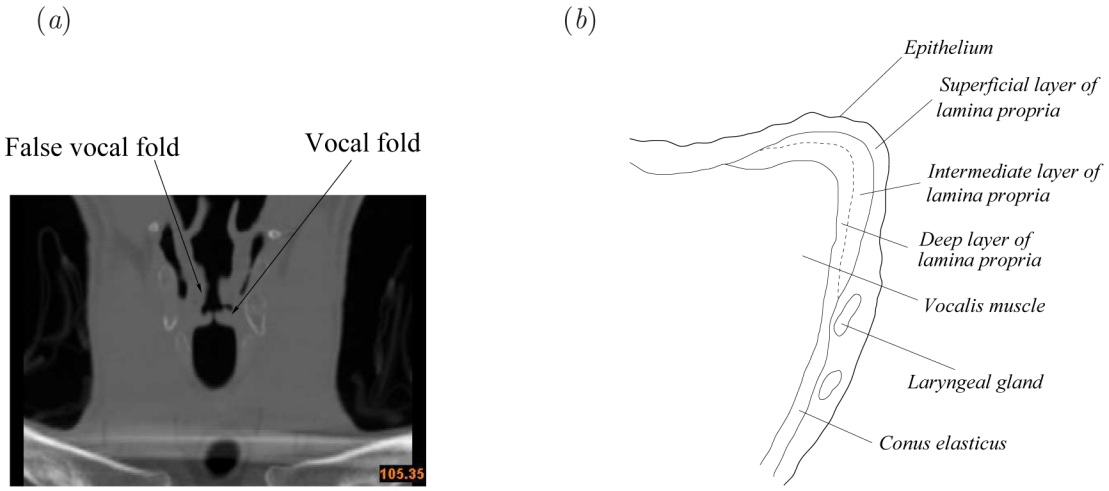

Figure 1.

(*a*) A CT scan image of the human larynx (coronal view) taken at 105 mm from the subject's back, where the light regions represent tissues or cartilage, and the dark regions represent hollow spaces. (*b*) Schematic of the histological layers of the vocal fold of a human adult adapted from [17].

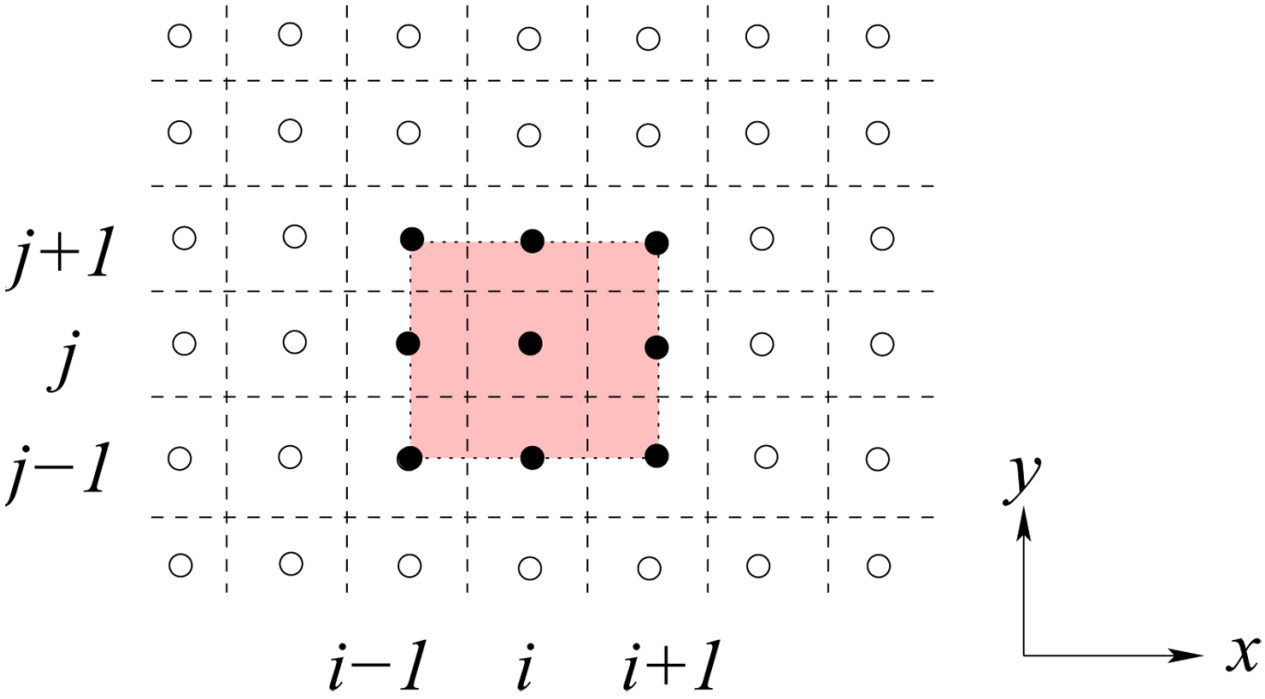

Figure 2.
The stencil that is used in the IB method to discretize the field equation at the collocation point (*i*, *j*). The nodal points involved in the stencil are marked with filled circles, while other nodal points are marked with unfilled circles.

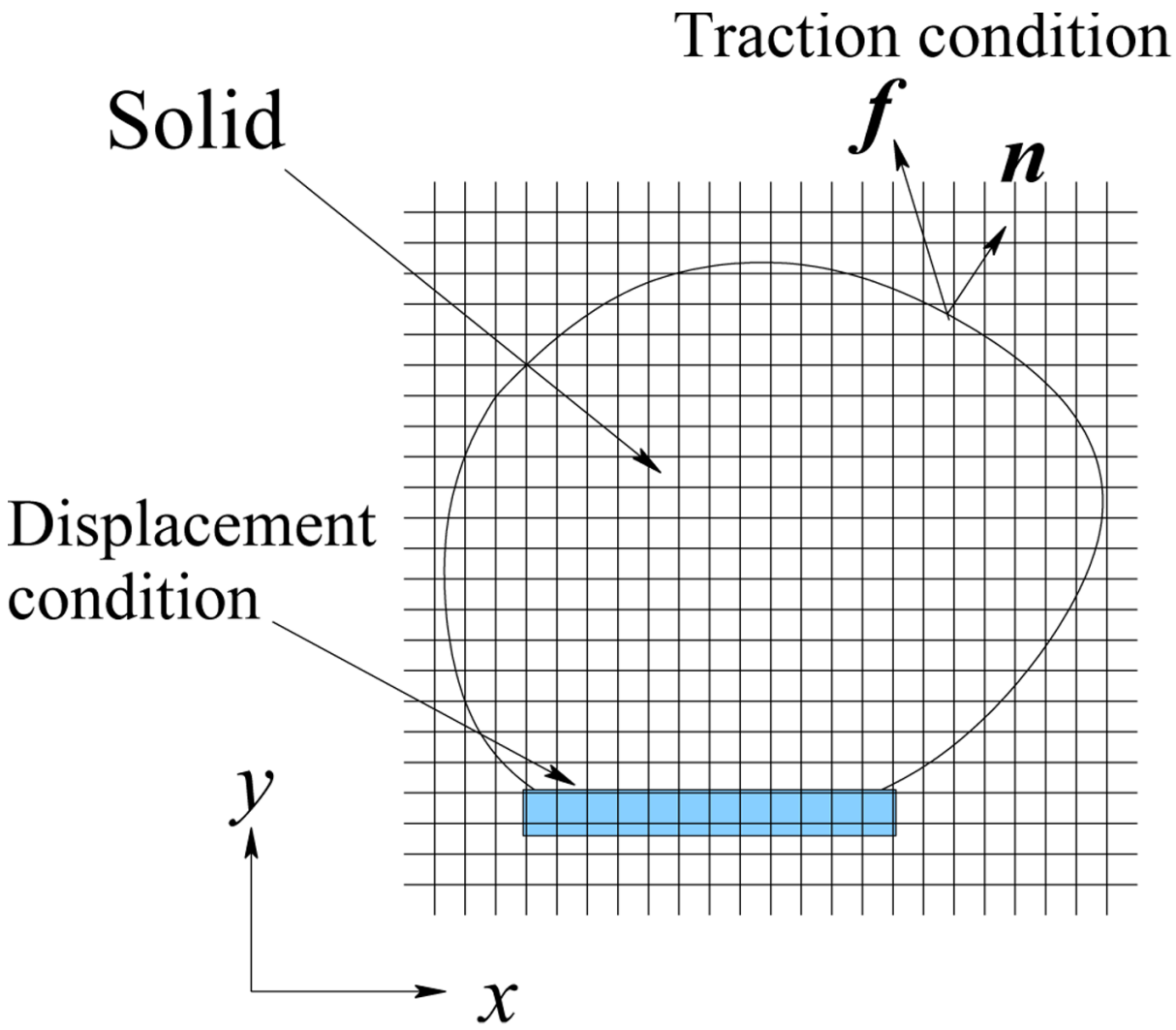

Figure 3.
The Cartesian grid that "immerses" a deformable body.

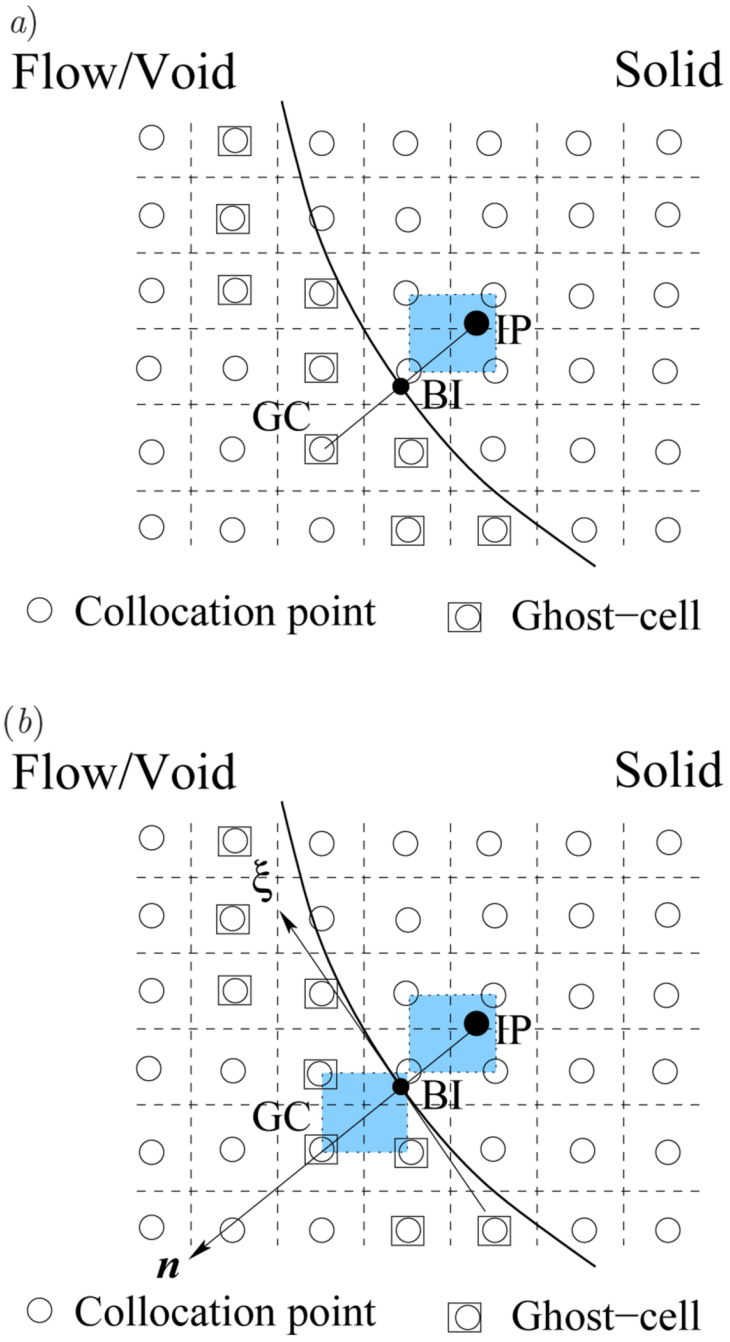

Figure 4.
Schematic of the immersed-boundary method on a Cartesian grid for solving the linear viscoelasticity. The bold curve represents the boundary of the solid. The stencil is shown in (*a*) for the displacement boundary condition and in (*b*) for the traction boundary condition.

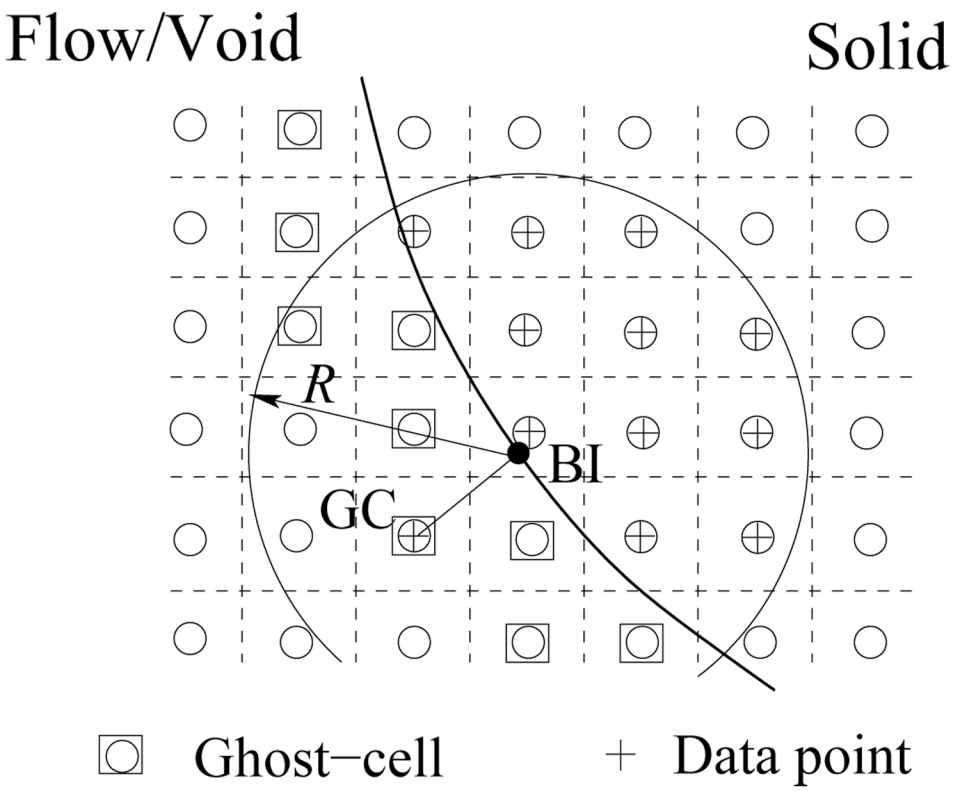

Figure 5.
Treatment of the traction boundary condition.

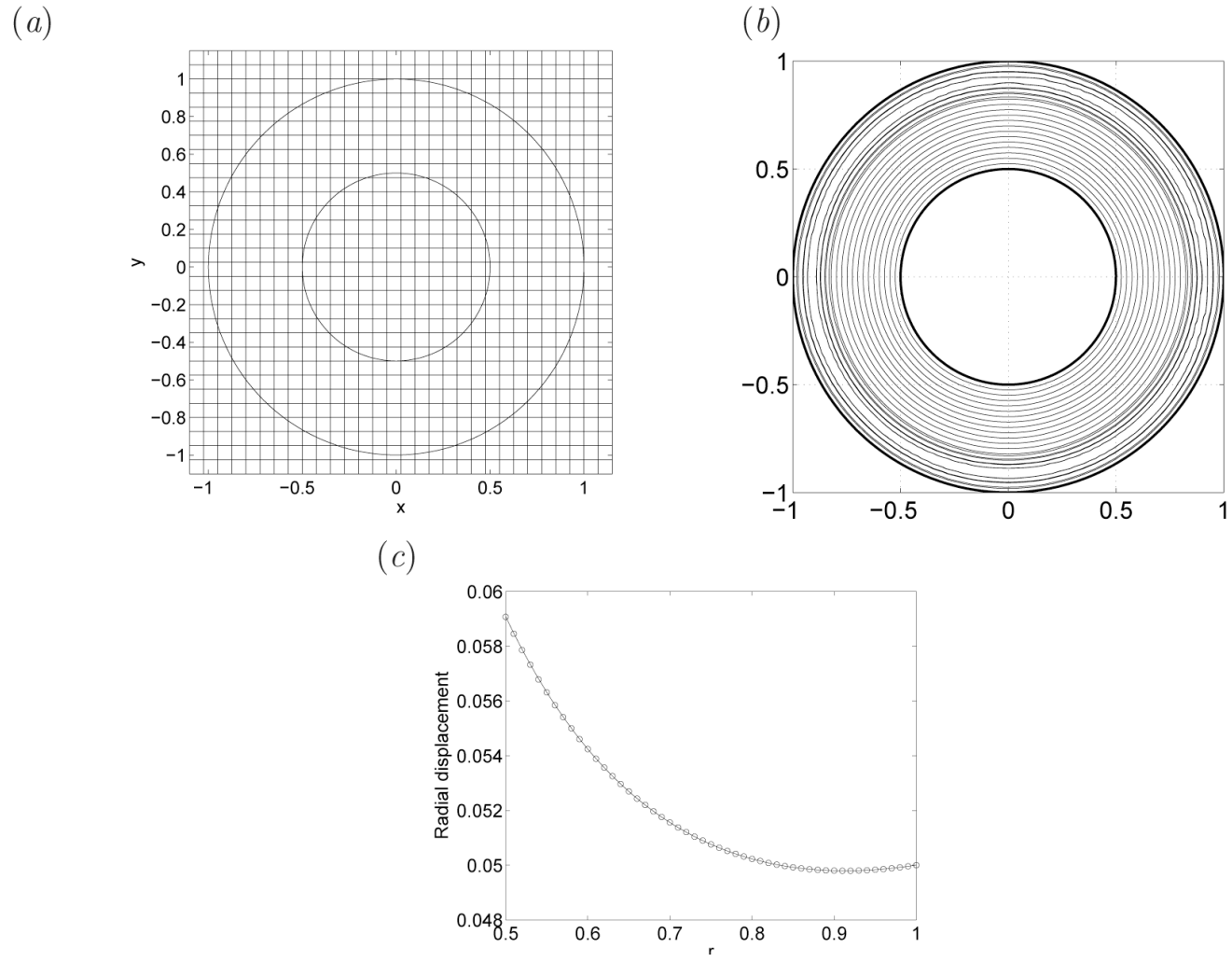

Figure 6.
(*a*) Annular linear-elastic solid immersed in a Cartesian grid. The solid is subject to a constant radial displacement on its outer boundary, and a traction-free or zero displacement condition is applied on its inner boundary. Results are presented for the traction-free case. (*b*) Contours of the radial displacement computed using the immersed-boundary method, where the bold lines represent the solid body. (*c*) The radial displacement as a function of *r* (solid line: exact solution; circles: numerical solution).

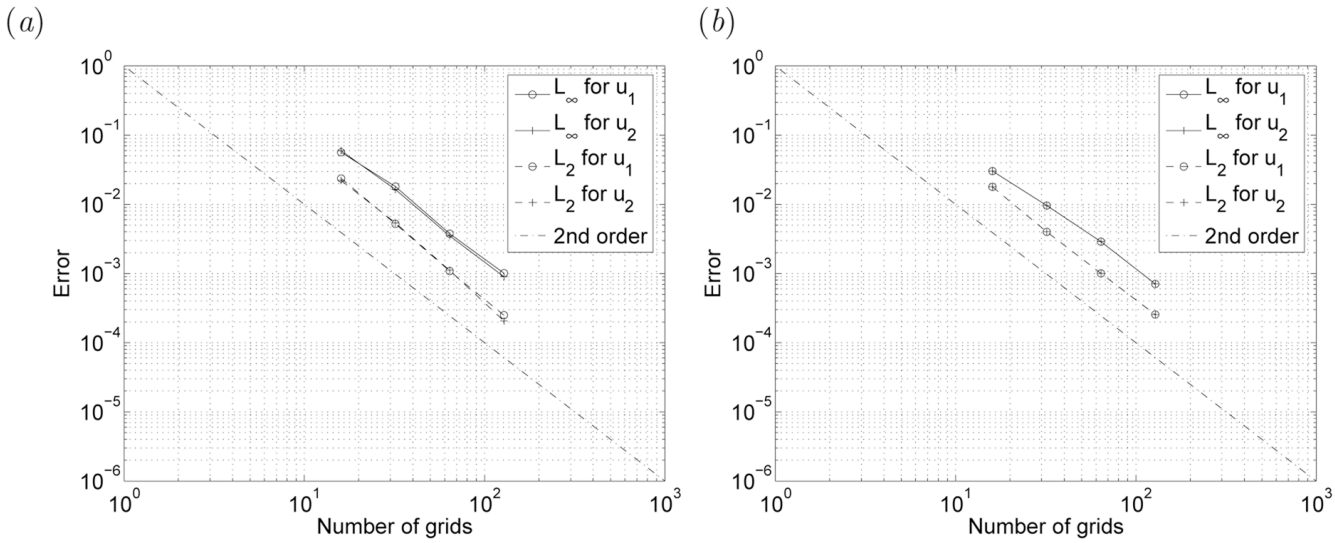

Figure 7.
Error norms of the solution obtained using the immersed-boundary method for the plane-strain annulus case with (*a*) traction-free inner surface and (*b*) fixed inner surface. The dash-dot line represents the second-order convergence rate.

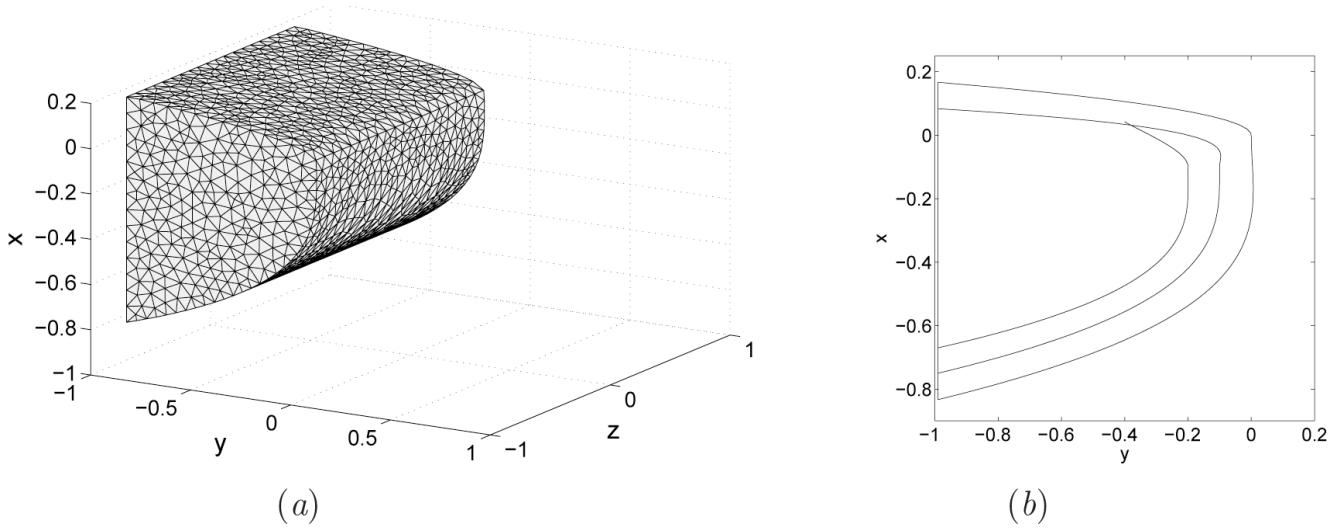

Figure 8.
(*a*) A 3D view of the vocal fold model. (*b*) The coronal section which consists of, from outside, the cover, the ligament, and the body. The length unit is centimeter.

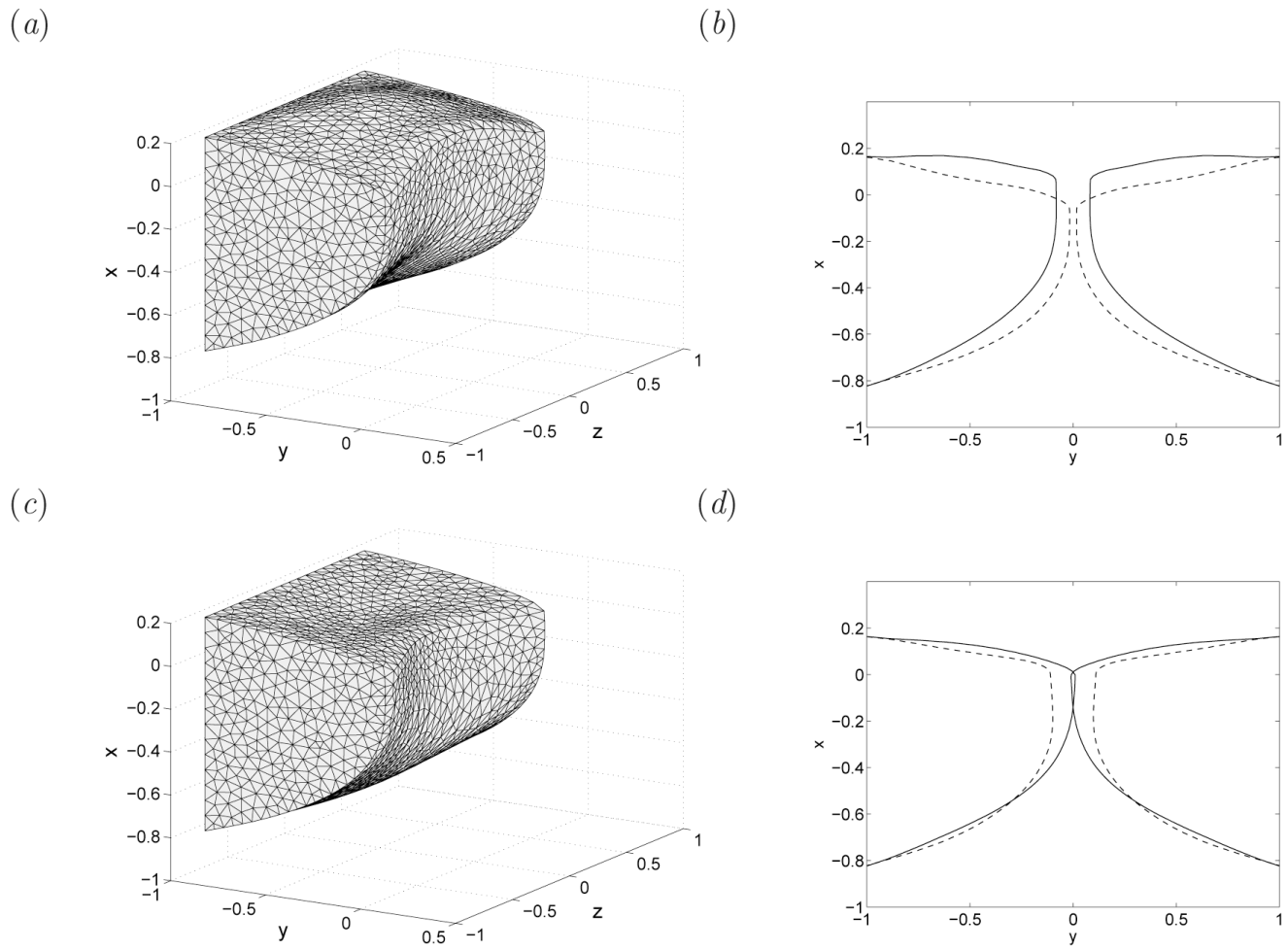

Figure 9.
The eigenfunctions of first two modes (left panel) and corresponding deformations in the mid-plane (right panel). (*a*, *b*) Mode-1, 114 Hz; (*a*, *b*) mode-2, 125 Hz;

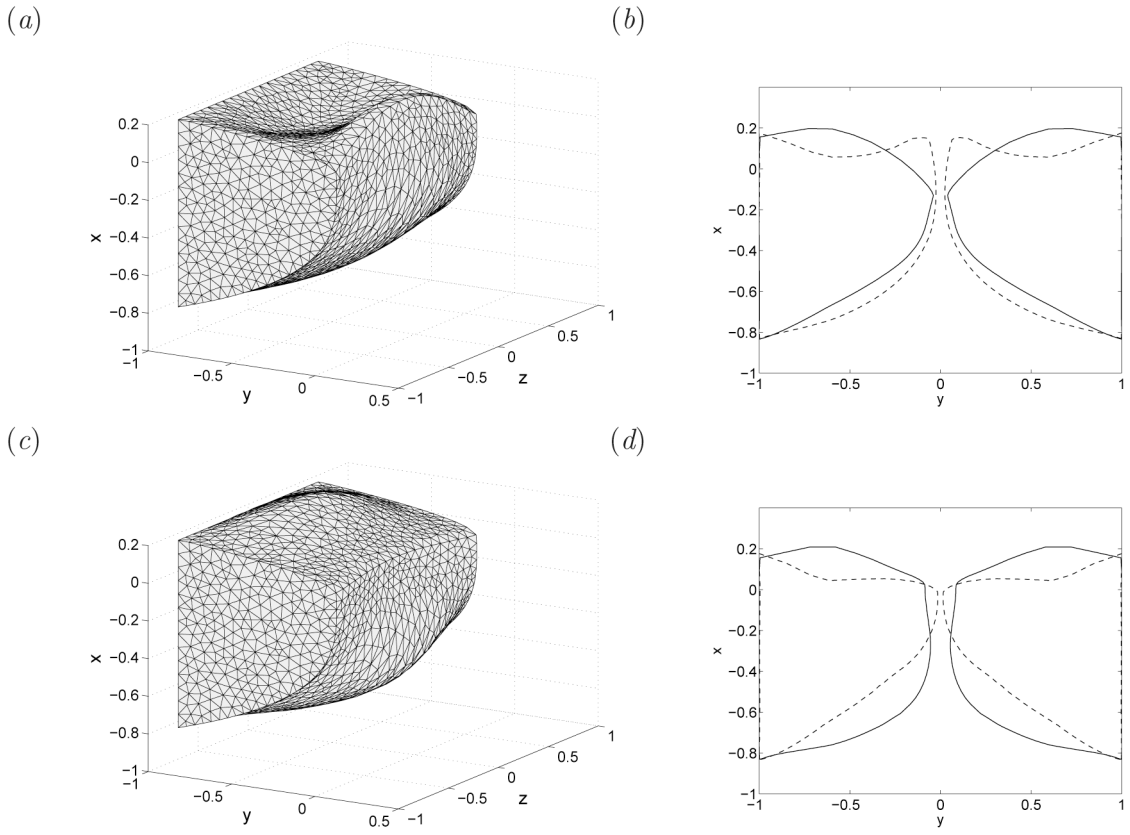

Figure 10.
The eigenfunctions of mode-3 and 4 (left panel) and corresponding deformations in the mid-plane (right panel). (*a*, *b*) Mode-3, 133 Hz; (*a*, *b*) mode-4, 144 Hz;

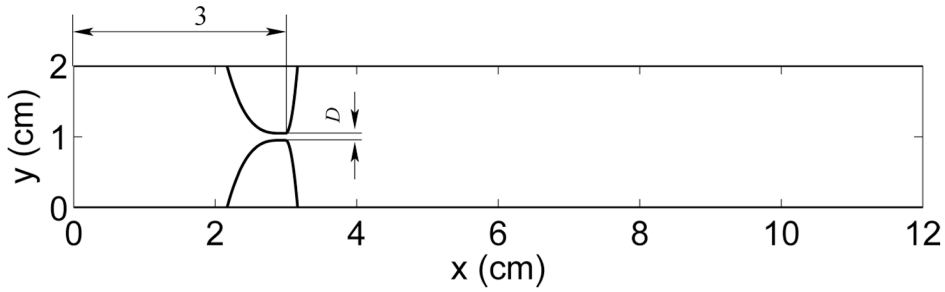

Figure 11.
The flow domain in present simulations of the glottal dynamics.

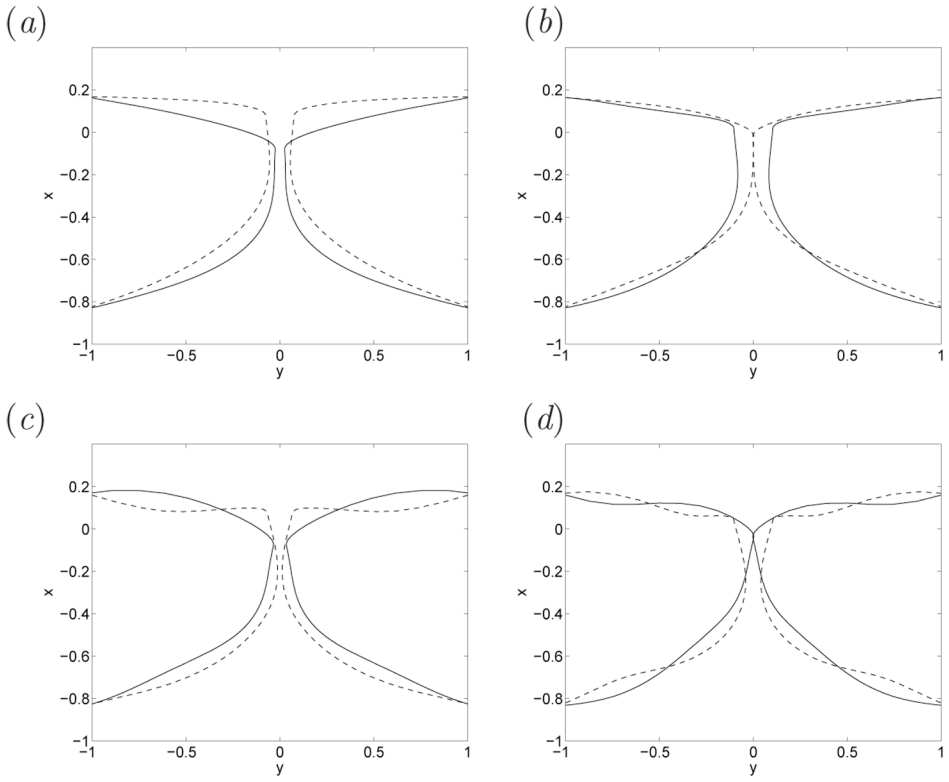

Figure 12.
The lowest four eigenmodes of the 2D vocal folds obtained using the immersed-boundary method. The associated frequency is (*a*) 94 Hz, (*b*) 215 Hz, (*c*) 247 Hz, and (*d*) 424Hz.

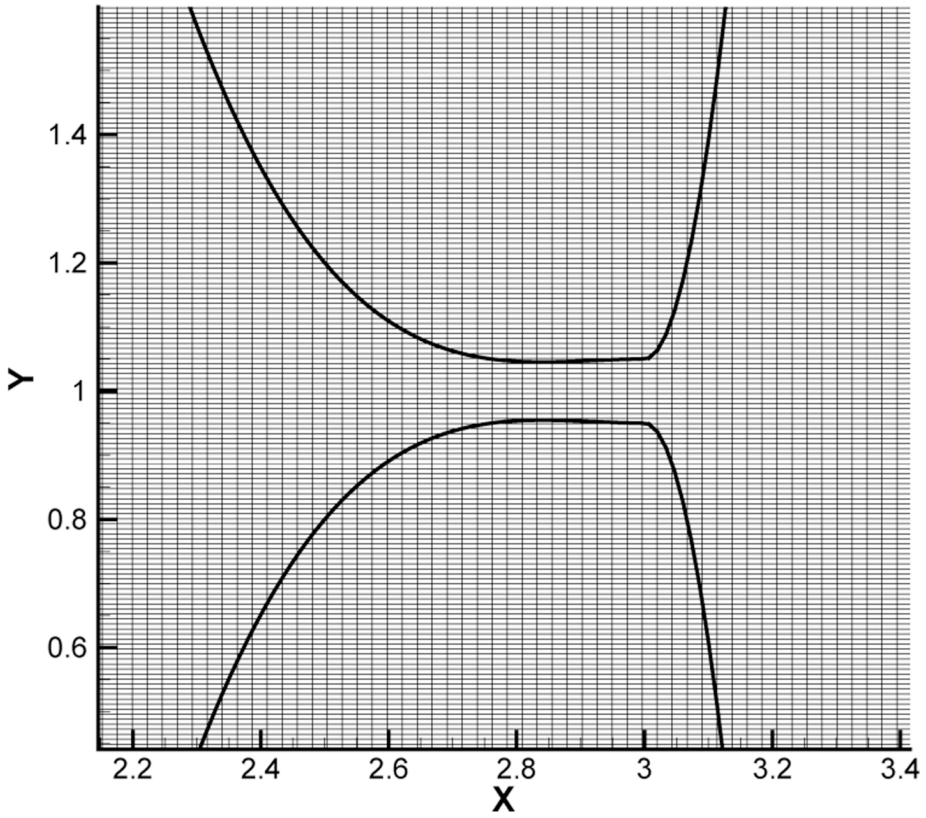

Figure 13.
The Cartesian grid around the glottis used for the flow simulation.

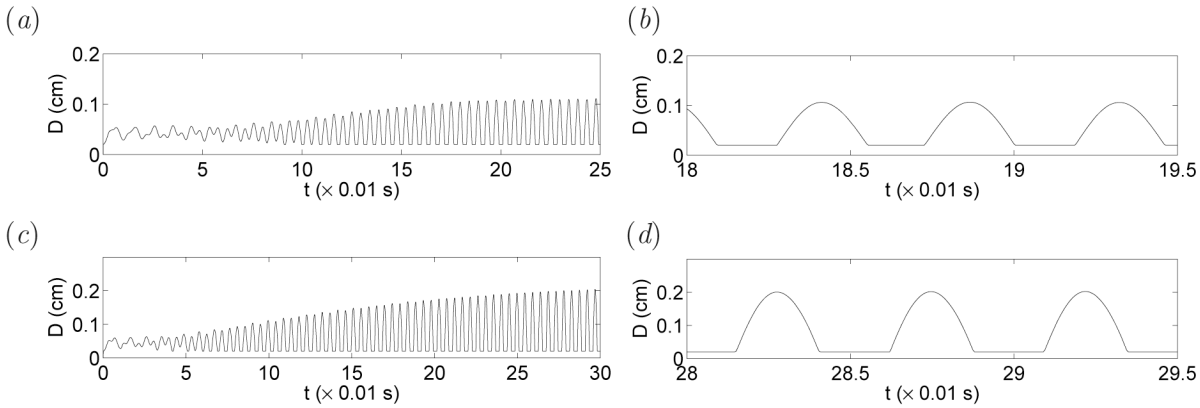

Figure 14.
History of the gap width, D (cm), during the induced vocal fold vibration. The close-ups are shown in the right panel. (*a*, *b*) η = 10 p; (*c*, *d*) η = 6 p.

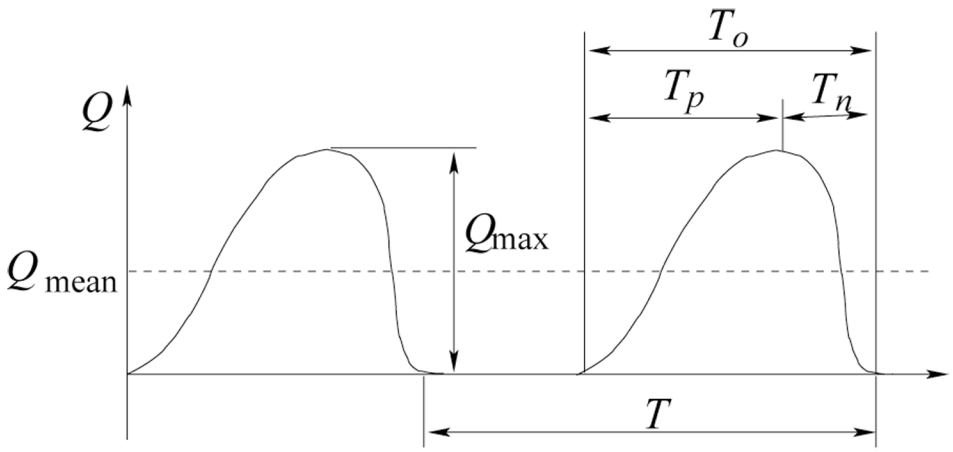

Figure 15.
Schematic of the glottal waveform of the volume airflow during phonation, adapted from [18].

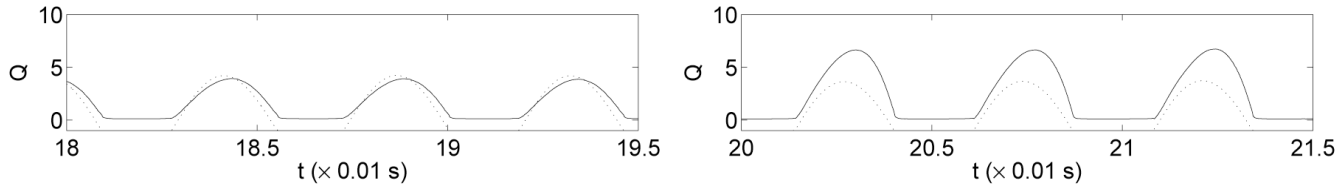

Figure 16.
History of the volume flux, Q (100 cm^2/s), for the induced vocal fold vibration. (*a*) η = 10 p; (*b*) η = 6 p. The dotted line represents the phase of the glottal gap.

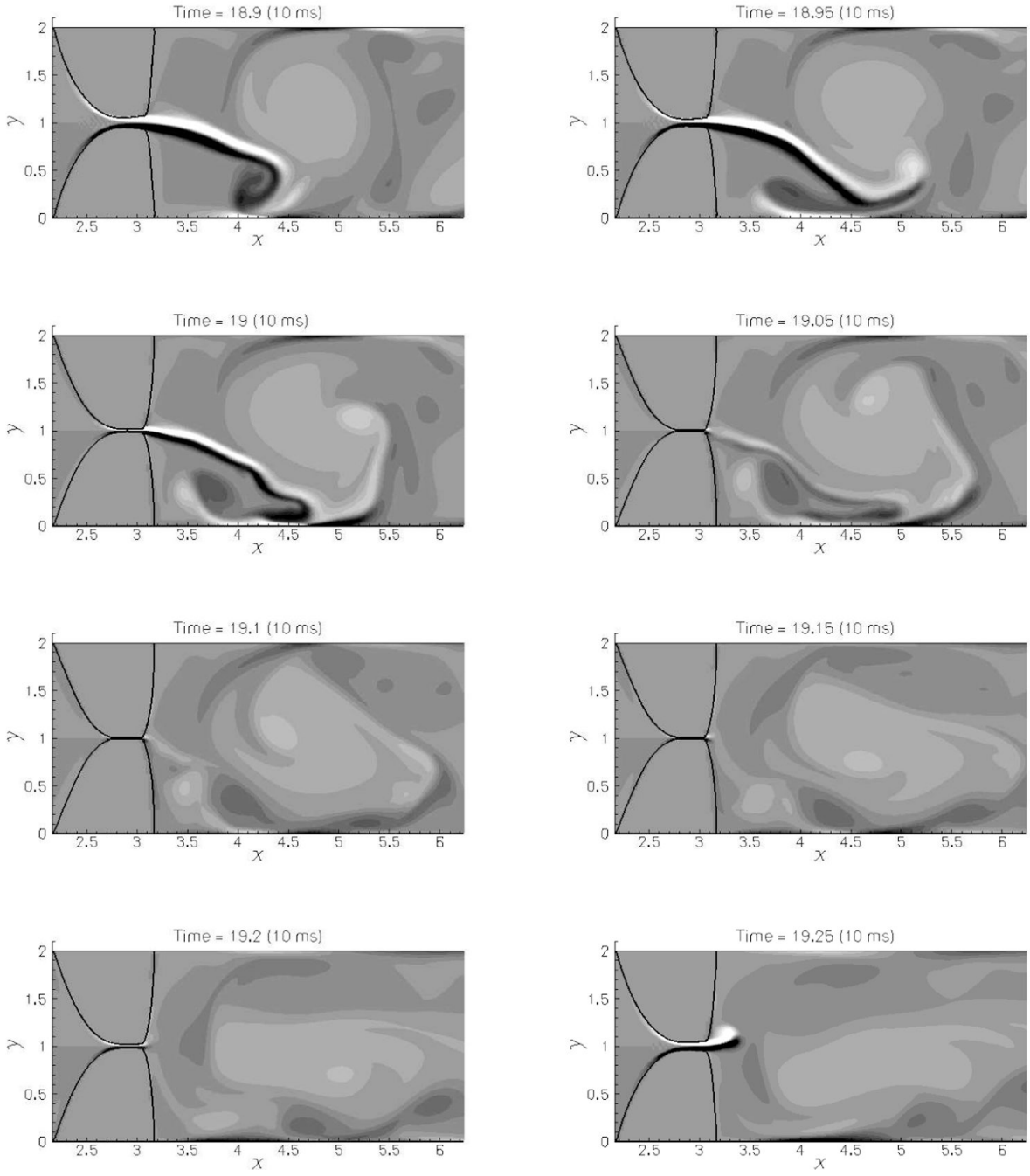

Figure 17.
Instantaneous vorticity contours between t = 18.90 cs and t = 19.25 cs for η = 10 p.

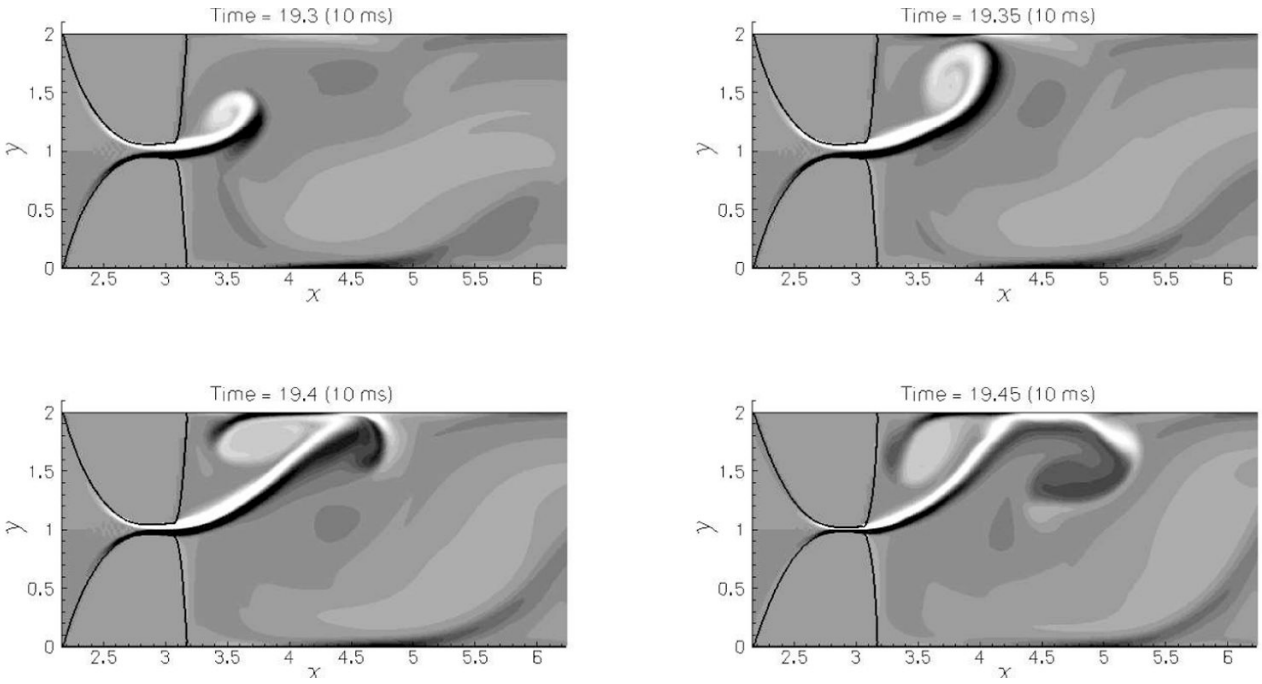

Figure 18.
Instantaneous vorticity contours between t = 19.30 cs and t = 19.45 cs for η = 10 p.

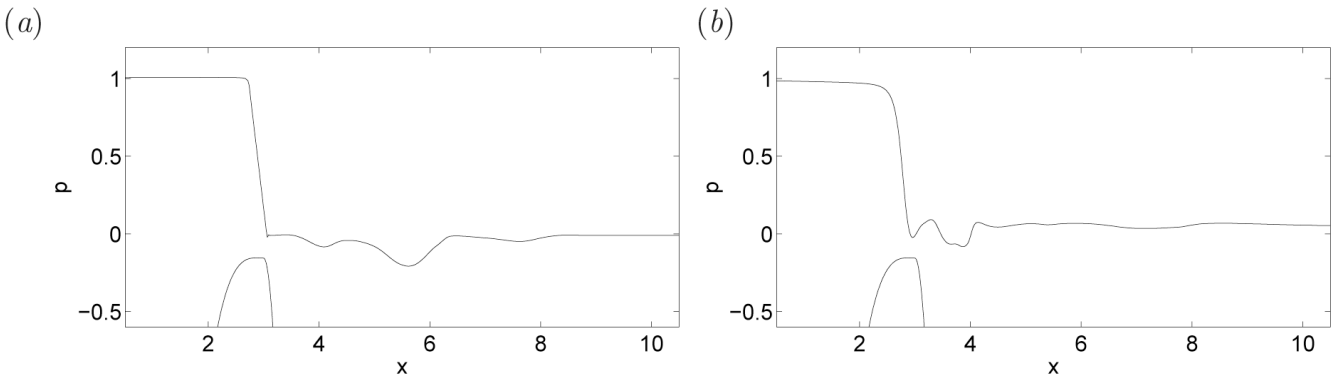

Figure 19.
Gage pressure (kPa) along the centerline of the channel for η = 10 p. (*a*) *t* = 18.20 cs (closure phase) (*b*) *t* = 18.40 cs (open phase). The streamwise position of the vocal fold is also shown.

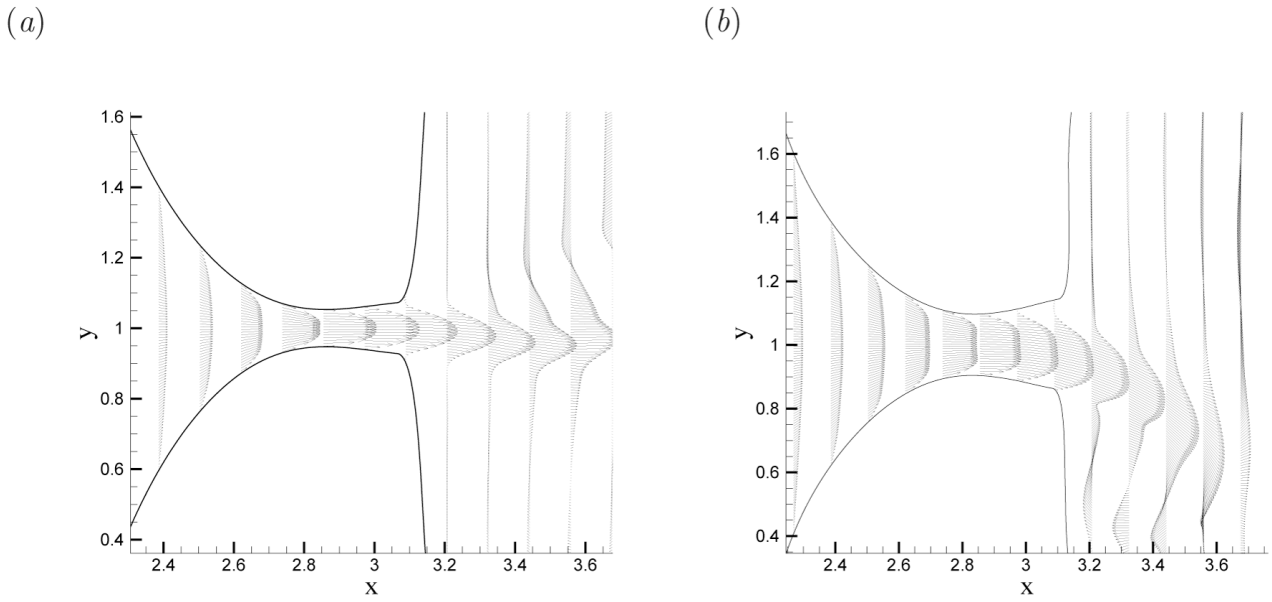

Figure 20.
Instantaneous velocity field around the glottis duing the open phase for (*a*) η = 10 p and (*b*) η = 6 p. Only partial grid points are shown.

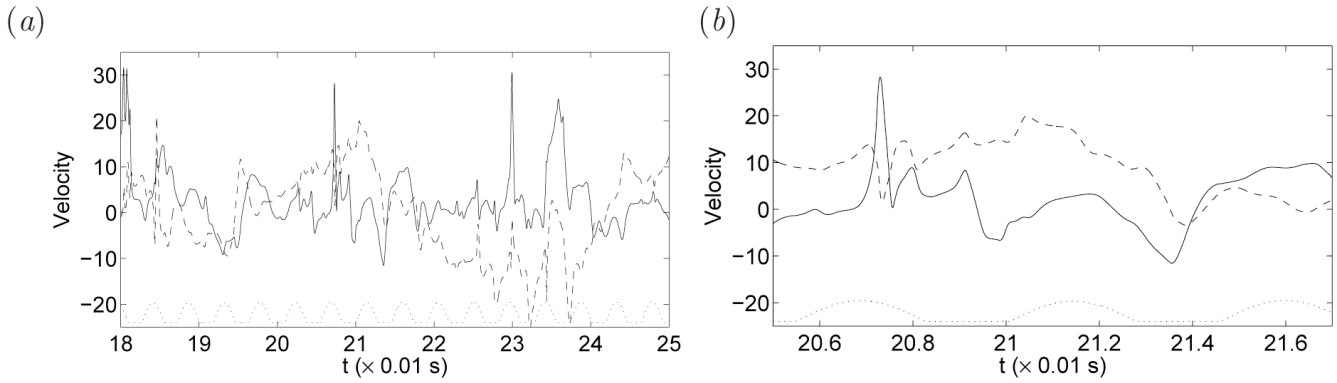

Figure 21.
Histories of v_1 (m/s) (solid lines) and v_2 (dashed lines) at $x = 4.5$ cm on the centerline. A close-up is shown in (*b*). The dotted lines represent the phase of the glottal gap.

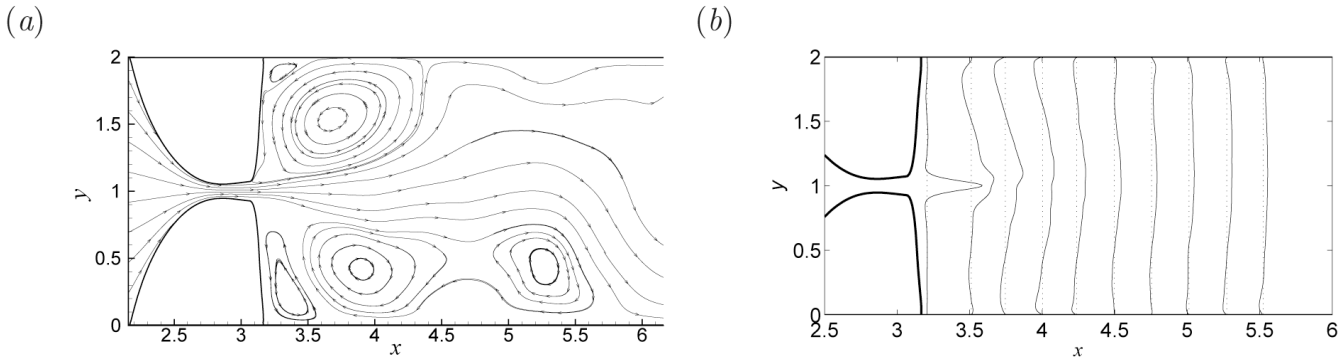

Figure 22.
Averaged flow field between $t = 18$ cs and $t = 25$ cs for $\eta = 10$ p. (*a*) Streamlines; (*b*) v_1 velocity profiles at different locations. Every 1 cm represents a velocity of 50 m/s.

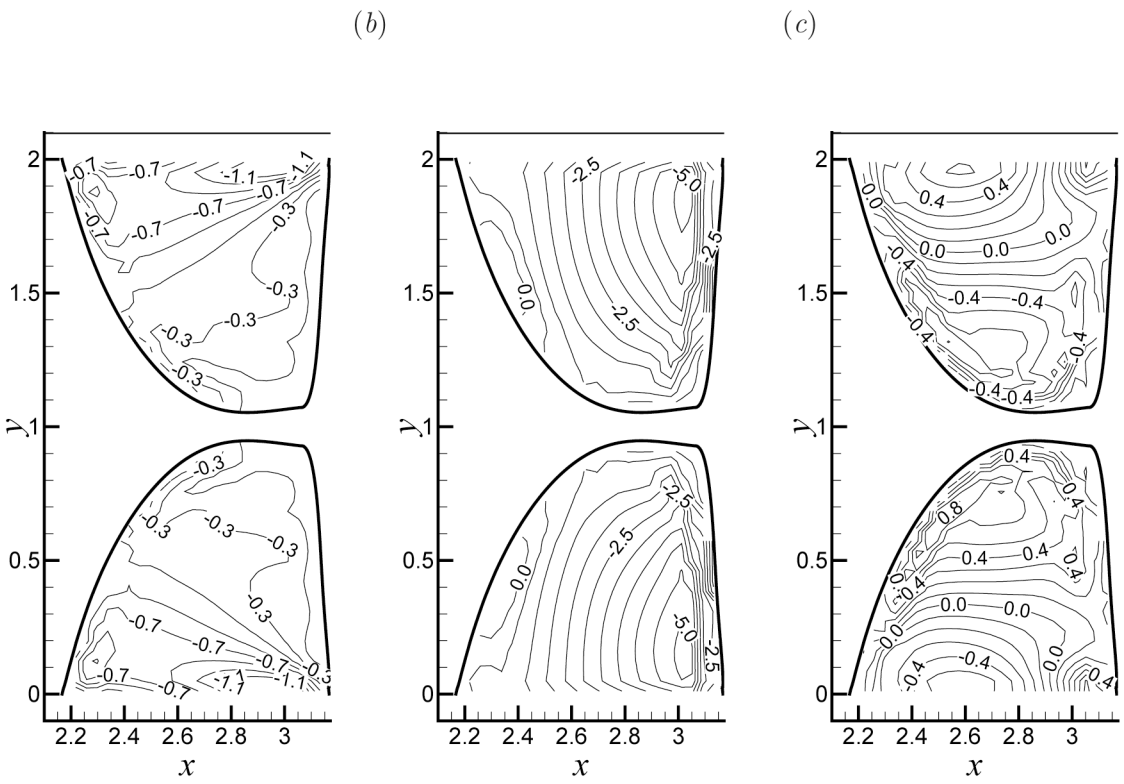

Figure 23.
Stresses in the vocal folds as they are fully open (η = 10 p). (*a*) σ_{xx}; (*b*) σ_{yy}; (*b*) σ_{xy}.

Table 1

Material properties of the three vocal fold tissue layers.

	μ_D	μ_{yz}	E_y	ν_D	ν_{xD}	ρ_s
Body	1.05 kPa	12 kPa	31.2 kPa	0.30	0.31	1.0 g/cm^3
Ligament	0.87 kPa	40 kPa	104 kPa	0.30	0.31	1.0 g/cm^3
Cover	0.53 kPa	10 kPa	26 kPa	0.30	0.31	1.0 g/cm^3

Table 2

Material properties of the tissue layers for the two-dimensional isotropic vocal fold model.

	μ_b	μ_{mz}	E_f	ν_b	ν_m	ρ_s
Body	20 kPa	20 kPa	52 kPa	0.3	0.3	1.0 g/cm^3
Ligament	40 kPa	40 kPa	104 kPa	0.3	0.3	1.0 g/cm^3
Cover	10 kPa	10 kPa	26 kPa	0.3	0.3	1.0 g/cm^3

Table 3

The grid distribution in the x direction for the flow simulation. The entries in parentheses are for the refined grid. In the y direction, 256 (384 for the fine grid) uniform grid points are used.

	Region I	Region II	Region III
Range	$0 \le x \le 2$ ($0 \le x \le 2$)	$2 \le x \le 5$ ($2 \le x \le 4$)	$5 \le x \le 12$ ($4 \le x \le 12$)
Number of grids	54 (64)	128 (192)	106 (128)
Δx	0.0234 ~ 0.0736 (0.0104 ~ 0.1131)	0.0234 (0.0104)	0.0234 ~ 0.2299 (0.0104 ~ 0.3440)

Table 4

Characteristics of the glottal waveform. The time unit is cs (0.01 second), and the flow-rate unit is 100 cm^2/s.

η	T	T_o	T_p	T_n	Q_{max}	Q_{mean}	τ_0	τ_s	q_r
10 p	0.456	0.28	0.16	0.12	4.0	1.57	0.61	1.33	0.39
10 p (fine grid)	0.463	0.29	0.16	0.13	4.0	1.58	0.63	1.23	0.40
6 p	0.473	0.26	0.16	0.10	7.6	2.68	0.55	1.60	0.35